國立臺灣大學電機資訊學院光電工程學研究所
碩士論文
Graduate Institute of Photonics and Optoelectronics
College of Electrical Engineering and Computer Science
National Taiwan University
Master’s Thesis

模擬分析包含與不包含振幅資訊光學相位共軛技術於散射介質中之聚焦效果

Simulation Analysis of Light Refocusing Through Scattering Media via Optical Phase Conjugation With and Without Amplitude Information

姚勝鈞
Sheng-Chun Yao

指導教授：曾雪峰 博士
Advisor: Snow H. Tseng, Ph.D.

中華民國 114 年 6 月
June, 2025

doi:10.6342/NTU202501087

誌謝

短短兩年的碩士路途中，得之於人者實在太多太多。如今回望，我懷著滿心的感恩提筆，寫下這篇誌謝。雖僅有寥寥數語，我仍真心期盼，諸位能感受到那滿溢於字裡行間，最誠摯的感激之情。

感謝家父與家母始終是我最堅強的後盾。在大學到研究所的六年中，提供我經濟上的支持，讓我能夠專注於學業，不需為生活而煩惱。在我挫折迷茫時，也給予我安慰與鼓勵，讓我知道身後永遠有一個溫暖的家。能成為你們的孩子，是我這輩子最大的幸福。

感謝雪峰老師兩年來的指導。在老師的帶領下，我一步步完成研究，並有幸首次參與國際研討會，這些經歷大大拓展了我的學術視野。研究之餘，老師在生活上的許多關心，讓我感受到無比的溫暖；對未來路途的悉心提點，更讓我受益匪淺。我深深感激老師給我這個機會，讓我能夠加入實驗室並在這裡成長。

感謝人瑋學長在研究上給予我許多的幫忙。與學長一同做研究，讓我從中學到許多身為研究員應具備的素養、技術與思考模式。同時，也感謝學長無私地分享自身寶貴經驗，讓我收穫良多。在這兩年中能夠遇見學長，是何其幸運。

感謝 425 實驗室夥伴：艾音、昱云學姊，李昊學長，姵潔、詩辰、瑋芸、立安、懷槿、珉瑄，柏逸、茗棋學弟，嘉妤學妹。謝謝你們為這兩年的實驗室生活注入滿滿的活力與笑聲，也總能在低落時互相扶持、勉勵。碩士生活中的每一段時光，無論喜悅還是低潮，因為與你們同行，都變得更加美好。

感謝我的摯友們：展昱、兆霖、逸翔。每次與你們聊天，我都能在歡笑與輕鬆中獲得無窮的能量，讓我在忙碌與壓力中重新找回平衡。你們的陪伴，不僅讓這趟碩士之旅充滿歡樂，也在我想停下腳步時，給予我再次前行的力量。

最後，我想謝謝這一路走來的自己。 ”Epsilon contributions complete an integral.” 感謝這兩年來每天都做出微小進步的你，因為你的努力堅持，我才能走到這個重要的檢查點。未來的路途，我也會一步一步，踏實地走完！

doi:10.6342/NTU202501087

中文摘要

在本研究中，我們採用時域擬譜法（Pseudospectral Time-Domain Method, PSTD）來模擬光在散射介質中利用包含與不包含振幅資訊光學相位共軛技術（Optical Phase Conjugation, OPC）回聚的情況，並將這兩種技術分別稱為精確振幅（Exact Amplitude, EA）OPC 和常數振幅（Constant Amplitude, CA）OPC。我們針對不同的散射體密度進行 EAOPC 和 CAOPC 的模擬，並對結果進行分析，以比較在不同散射條件下這兩種技術的差異。研究結果顯示，在相同的散射體數量密度下，EAOPC 的表現優於 CAOPC，但隨著散射體密度增加，其表現會下降。進一步的研究結果表明，CAOPC 可以應用於密集介質中，但在稀疏介質中則不適用。最後，本文也討論了這些現象背後的原因。本研究為在散射介質中操控光提供了重要見解，並希望能為生物組織中的光學應用做出貢獻。

關鍵字：光學相位共軛（Optical Phase Conjugation, OPC）、散射介質、波前整形（Wavefront Shaping）、時域擬譜法（Pseudospectral Time-Domain Method, PSTD）

ABSTRACT

We employ the pseudospectral time-domain (PSTD) method to model light refocusing through scattering media using optical phase conjugation (OPC) with and without amplitude information, referred to as exact amplitude (EA) OPC and constant amplitude (CA) OPC, respectively. Simulations of EAOPC and CAOPC are conducted across various scatterer number densities, followed by an analysis of the results to identify the differences between the two techniques under varying scattering conditions. Our results show that EAOPC outperforms CAOPC under the same scatterer number density, but its performance declines with increasing scatterer number density. Research findings further demonstrate that CAOPC is applicable in dense media but not in sparse media. Finally, the reasons behind these phenomena are also discussed. This research provides important insights into manipulating light propagation in scattering media and hopes to advance optical applications in biological tissues.

Keywords: optical phase conjugation (OPC), scattering media, wavefront shaping, pseudospectral time-domain (PSTD) method

doi:10.6342/NTU202501087

CONTENTS

doi:10.6342/NTU202501087

doi:10.6342/NTU202501087

LIST OF FIGURES

doi:10.6342/NTU202501087

LIST OF TABLES

doi:10.6342/NTU202501087

Chapter 1 Introduction

Random light scattering often limits optical techniques in biological tissues [1-4]. Diagnostic applications such as optical imaging methods suffer from distortion due to the loss of focus caused by light scattering in turbid tissues. Similarly, therapeutic applications are also hindered by the scatterers in biological tissues. Phototherapy, for instance, relies on transmitting highly focused optical power to the targeted diseased area. However, light scattering within biological tissues attenuates the energy delivery to the targeted region, reducing therapeutic efficacy. These examples illustrate that light scattering is a significant barrier to effective light focusing in biological tissues, failing diagnostic and therapeutic optical applications. Addressing this challenge is essential and could lead to substantial advancements in biophotonics technologies.

Optical phase conjugation (OPC) solves this problem by manipulating the amplitude and phase of light [1-5]. When a continuous wave (CW) source emits waves that pass through a scattering medium, the scattered waves interfere to form a speckle pattern. An OPC region records this speckle pattern's amplitude and phase information, then turns each segment in the OPC region into a source with the same recorded amplitude and a phase conjugated to the recorded phase. Hence, as generated waves from the OPC region propagate back through the medium, the phases are canceled out, allowing the waves to interfere constructively at the CW source region and refocus the energy.

Furthermore, digital optical phase conjugation (DOPC) has created new avenues for directing light through scattering media [6-11]. It first receives the phase information of a speckle pattern from a feedback system. Then, it shines a beam with constant amplitude (CA) through a spatial light modulator (SLM) to shape the beam’s wavefronts into the

doi:10.6342/NTU202501087

phase-conjugated form of the feedback phase information. As the modulated beam passes through the scattering medium, the waves form constructive interference at the targeted point. This process reveals a phase-only OPC approach, which enables precise wavefront control without requiring explicit amplitude modulation, prompting our interest in the importance of amplitude information. Hence, we conduct pseudospectral time-domain (PSTD) simulations to explore the effectiveness of OPC refocusing in scattering media with and without amplitude information.

The PSTD method is a highly suitable numerical technique for simulating macroscopic light scattering problems [12, 13]. These problems often involve extensive scattering media and numerous irregular light scattering events, making traditional simulation methods difficult to apply. In contrast, due to its unique computational approach, the PSTD method effectively reduces computational resource consumption while maintaining high accuracy. Therefore, the PSTD method is efficient and accurate for large-scale light scattering simulations [14, 15].

In this research, we employ the PSTD method to simulate OPC refocusing, using the exact amplitude (EA) information that the OPC region records and CA information, both combined with the recorded phase information, under varying scatterer number densities. We compare the results and analyze the variations of EAOPC and CAOPC. This research not only enhances our understanding of both techniques in different scattering conditions but also provides valuable insights into OPC. We hope this study can be a foundation for future research on manipulating light in scattering media, particularly in biological tissues.

In this thesis, we review the published literature related to the research in Chapter 2. Chapter 3 introduces the PSTD algorithm applied in this study. Chapter 4 presents the simulation results and subsequent discussion. Finally, we summarize the research and suggest future work in Chapter 5.

Chapter 2 Literature Review

This chapter summarizes the research relevant to this study, including OPC and numerical simulation methods for light scattering. In Section 2.1, we introduce OPC and its applications to guide light through scattering media. In Section 2.2, we organize common numerical modeling methods for light propagation in scattering media.

2.1 Optical Phase Conjugation

In 1961, P. A. Franken and coworkers in the Randall Laboratory at the University of Michigan observed the second harmonic generation for the first time [16]. This event launched a golden age in non-linear optics, and OPC was one of the new non-linear optical techniques. Since then, OPC has been widely researched and continues to be studied today.

OPC is known for its ability to reverse the propagation direction of a wave with a conjugated phase. This can be accomplished through three primary methods: the stimulated Brillouin scattering process, the one-photon or multi-photon pumped stimulated emission process, and the four-wave mixing technique. A device that generates the phase conjugation effect is referred to as a phase conjugate mirror (PCM). The entire process of OPC and the distinction between a PCM and a standard mirror are shown in Fig. 2.1. Once a wave interacts with a PCM, its propagation direction inverts, and its phase becomes conjugated. The backward wavefront duplicates the shape of the forward wavefront while reversing its propagation direction. This suggests that the forward wavefront undergoes a time-reversal process. The significant time-reversal feature of OPC has opened up new opportunities across various fields [17, 18].

doi:10.6342/NTU202501087

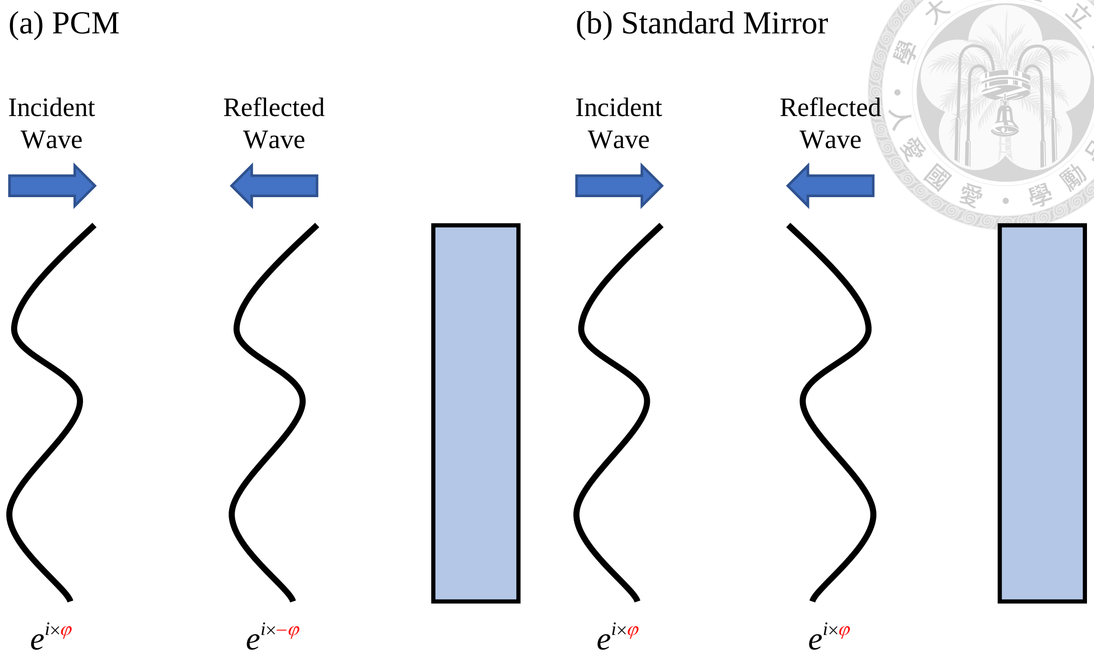

Fig. 2.1 A schematic of a wavefront impinging on (a) a PCM and (b) a standard mirror. Comparing (a) with (b), the wavefront impinging on the PCM preserves the same shape as the incident wavefront, revealing the time-reversal characteristic of OPC.

One prominent application of the time-reversal feature is overcoming random light scattering in biophotonics [1-5]. When waves propagating through a scattering medium undergo a time-reversal process, they effectively retrace their original paths and return to their initial states as if the scattering medium had never affected them. Hence, the time-reversal feature restores scattered waves to their original states, eliminating the random light scattering effect.

Here, we further explain this concept with Fig. 2.2. Consider a CW source emitting waves traveling toward a scattering medium. As the waves pass through the medium, their wavefronts become distorted. After impinging on a PCM, the distorted wavefronts are transformed into their time-reversed forms. When these time-reversed wavefronts travel back through the same scattering medium, they recover their original forms, and the waves refocus at the CW source region.

This process can be interpreted from a wave-optical perspective. The distorted wavefronts create a speckle pattern on the PCM through interference. The PCM then records the amplitude and phase information of this speckle pattern and turns each segment of it into a source with the EA recorded by the PCM and a phase conjugated to the recorded phase. The waves emitted from all these sources reconstruct the time-reversed forms of the distorted wavefronts. As the phases are canceled by propagating through the same scattering medium again, the time-reversed wavefronts are corrected to their original forms, and the waves constructively interfere at the CW source region, which refocuses the light.

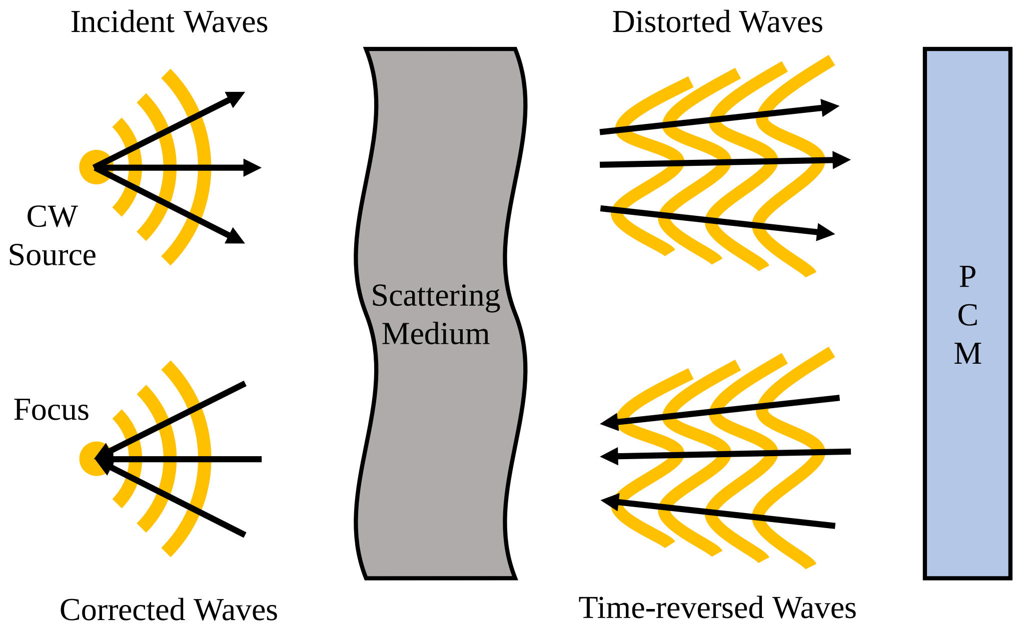

Fig. 2.2 A schematic of OPC light refocusing through a scattering medium. The time-reversal property of OPC returns distorted waves to their original states, successfully refocusing the waves.

OPC is often integrated with a charge-coupled diode (CCD) camera and an SLM, which creates a field of DOPC. By placing a CCD camera at a targeted point, the CCD camera captures information passing through a scattering medium. Then, the CCD camera sends the information back to an SLM as a feedback signal to optimize the phase. The optimization scheme is to compensate for phase distortions, which is mathematically equivalent to OPC. Finally, a CA beam passes through the SLM, and the wavefronts from each pixel of the SLM are optimized, forming constructive interference at the targeted point. I. M. Vellekoop and co-workers first demonstrated this technique to direct light through a strongly scattering medium [6]. They then advanced the method by focusing fluorescence in turbid tissues [8]. Meng Cui and Changhuei Yang further investigated the DOPC system's design and robustness [7], followed by recent developments from Pidong Wang and colleagues [11]. In 2022, Linxian Liu et al. introduced a full-polarization DOPC approach, which simultaneously modulates orthogonally polarized optical field components and enhances light refocusing capabilities [9]. Most recently, YoonSeok Baek and co-workers presented a DOPC method for spatially incoherent light, enabling light focusing through emissions from multiple spatially separated targets. [10].

In addition, OPC can be combined with ultrasound methods, which is time-reversed ultrasonically encoded (TRUE) optical focusing. Xiao Xu and colleagues significantly advanced this field by utilizing an acousto-optic technique [19]. They simultaneously exposed a sample to light and focused ultrasound waves. At the ultrasound focus within the scattering medium, the light was modulated and underwent a frequency shift. As a result, the ultrasound focal point effectively became a source of frequency-shifted light. Then, they isolated the frequency-shifted light from the unshifted light, applied OPC, and redirected it back to the focal point. In 2021, Zhongtao Cheng and Lihong V. Wang reported a new ultrasound-assisted technique based on TRUE optical focusing, which is ultrasound-induced field perturbation (UFP) optical focusing [20]. By calculating the difference between light fields through a scattering medium with and without focused ultrasound waves, the researchers directly extracted the diffracted light from the focal point of the ultrasound waves. Conventional TRUE optical focusing can only take

doi:10.6342/NTU202501087

advantage of frequency-shifted light (the first order), but UFP optical focusing can utilize the unshifted light (the zero order), leading to superior performance to conventional TRUE optical focusing.

With a focus in scattering media, the researchers could apply it to imaging. Chia-Lung Hsieh et al. placed a nanoparticle layer and a scattering medium layer together. Due to the nonlinear optical properties of the nanoparticle, when an infrared laser pulse stimulated it, the nanoparticle generated light with double the frequency. This light, after passing through the scattering medium, was recorded using DOPC and then refocused to the nanoparticle's original location. By scanning the focus across the nanoparticle layer, they were able to image its surrounding environment [21]. Similarly, Ying Min Wang and co-workers demonstrate the deep-tissues imaging by the TRUE system [22]. Tumor microtissues were embedded in a layer of fluorescent quantum dot gel, positioned between two 2.5 mm-thick pieces of chicken tissue. To generate the image, the ultrasound focus was scanned across the plane, and at each scan position, an optical focus created through phase conjugation stimulated fluorescence. By measuring the fluorescence from different focal points, they successfully constructed an image of the tumor microtissues.

On the other hand, a focus within scattering media also helps energy transmission to biological tissues, enhancing phototherapy applications. Photodynamic therapy is a well-established example. Photodynamic therapy demands activating a pre-administered photosensitizing drug by illuminating the targeted diseased area. With a focus on the drugs, energy can be delivered entirely, preventing energy attenuation caused by light scattering. Therefore, the drug can be completely activated, significantly increasing the efficacy. A focused beam is also beneficial in tissue ablation. Focusing light in deep tissues can lead to deeper tissue ablation, extending accessible tissue ablation regions. Additionally, highly focused optical power allows the energy to concentrate on a specific

doi:10.6342/NTU202501087

tissue while minimizing damage to surrounding areas. This precision leads to better therapeutic outcomes and reduces harm to untargeted tissues, improving the effectiveness of tissue ablation.

Based on the above discussion, we identified a key difference between conventional OPC and DOPC: the presence or absence of amplitude information in the OPC light refocusing process. We also recognized that focusing light in scattering media creates a way for imaging and enhances energy transmission. Therefore, in this research, we investigate the OPC refocusing process with and without amplitude information, which deepens the understanding of OPC and contributes to its implementation in focusing light through scattering media, such as DOPC and TRUE.

2.2 Numerical Simulation Methods

Numerical simulations are crucial for research on optical diagnostic and therapeutic techniques as they require a thorough understanding of light scattering in biological tissues. Although simulations are less convincing than experiments, they allow us to easily turn off noisy sources, change variables, and analyze specific factor contributions. Thus, simulations complement experiments by revealing insights that are often difficult to observe in experiments, leading to a comprehensive investigation of certain phenomena. As a result, numerical simulation approaches are well-developed in the field of biomedical light scattering.

The Monte Carlo (MC) simulation is frequently applied to model light propagation in biological tissues [23, 24]. It treats the movement of a single photon as a series of multiple collisions with scatterers. Each time the photon encounters a scatterer, the simulation samples the probability distribution for angular deflection, determining the

doi:10.6342/NTU202501087

new direction of the photon. This process continues until the photon is eventually absorbed. By launching numerous photons in the simulation, the statistical behavior of the photons effectively predicts the scattering phenomenon in biological tissues.

However, due to its fundamental assumptions, the MC simulation fails to model wave-optical phenomena. Treating light scattering as a series of collision events oversimplifies light-matter interactions. Assuming photons propagate independently neglects coherent interference effects. These heuristic approaches overlook the electromagnetic wave essence of light, limiting the MC simulation's ability to describe wave-optical phenomena. Consequently, while the MC simulation is valuable for modeling photon transport in scattering media, it lacks the theoretical rigor necessary for modeling the OPC phenomenon, which requires precise wave-optical analysis [25].

To accurately model wave-optical phenomena, the finite-difference time-domain (FDTD) method is often employed. Combining the Yee grid with the central-difference scheme, the FDTD method discretizes Maxwell’s equations in both spatial and temporal domains and solves them numerically [26]. Currently, the FDTD method is widely utilized across various fields [27]. Andrew Dunn, Rebekah Drezek, and colleagues employed the FDTD method to explore light scattering from a single cell [28-30]. This marks the first attempt to examine light scattering characteristics in biological tissues by directly solving Maxwell’s equations.

Nonetheless, the FDTD method falls short in simulating light scattering in turbid media containing many scatterers. Due to the central-difference scheme used in the FDTD method, it usually requires 20 sampling points to reconstruct a wavelength in the spatial domain. As a result, the fine grid significantly reduces the efficiency of the FDTD method, especially in large-scale simulations. Hence, the FDTD method is unsuitable for simulating light scattering in a large cluster of scatterers.

doi:10.6342/NTU202501087

The PSTD method, derived from the FDTD method, is highly efficient for modeling large-scale problems. In 1997, Q. H. Liu first introduced the PSTD method for numerically solving Maxwell’s equations [31]. Since then, it has been widely applied to large-scale problems across various fields, including electromagnetic and acoustic measurement simulations and plasma simulations [14, 15]. The PSTD method has also been used to simulate light scattering and refocusing in turbid media via OPC for both pulse and continuous waves [12, 13]. These applications highlight the PSTD method's strong potential for solving large-scale problems.

The PSTD method can efficiently model large-scale problems because of a unique discretization approach. Unlike the FDTD method, which applies the central-difference scheme to both temporal and spatial discretization, the PSTD method retains the central-difference scheme for temporal discretization while utilizing the fast Fourier transform for spatial discretization. Therefore, its spatial sampling rate is governed by the Nyquist sampling theorem, enabling wavelength reconstruction with only two spatial samples. This allows the PSTD method to achieve high accuracy with a coarse grid, significantly reducing computational resources and enhancing efficiency in large-scale modeling.

In this research, we simulate light scattering in a large cluster of scatterers and refocusing via OPC. This problem is large-scale and involves wave-optical phenomena. The PSTD method preserves the wave properties of light by rigorously solving Maxwell’s equations while efficiently modeling large-scale problems using the fast Fourier transform in the spatial domain. Hence, the PSTD method is highly suitable for this study.

doi:10.6342/NTU202501087

Chapter 3 The PSTD Algorithm

This chapter introduces the PSTD algorithm and related topics. In Section 3.1, we first derive the basic update equations of the PSTD method. Then, in Section 3.2, we present the Nyquist sampling theorem, the key reason why the PSTD method is efficient in large-scale problems. Section 3.3 reviews numerical dispersion and the stability condition for the PSTD method. Section 3.4 details the strategy for implementing a simple soft source in PSTD simulations. Finally, in Section 3.5, we incorporate the perfectly matched layer (PML) absorbing boundary condition with the PSTD method. We hope this chapter serves as a manual for the PSTD algorithm.

3.1 The Basic Update Equations

The basic update equations, derived from discretizing Maxwell's equations, form the core algorithm of the PSTD method. In this section, we detail the entire discretization process. We start from continuous Maxwell's equations and discretize them in both temporal and spatial domains, finally arriving at the basic update equations of the PSTD method.

Faraday's law and Ampere's law in a source-free region can be written as Eq. (3.1) and (3.2), respectively.

$$\nabla \times \vec{E}(t) = -\mu \frac{\partial \vec{H}(t)}{\partial t} \tag{3.1}$$

$$\nabla \times \vec{H}(t) = \varepsilon \frac{\partial \vec{E}(t)}{\partial t} \tag{3.2}$$

Here, $\vec{E}$ and $\vec{H}$ denote the electric field vector and the magnetic field vector, respectively. μ and ε denote the permeability and the permittivity in matters, respectively.

In the temporal domain discretization, the central difference approximation is implemented to calculate these temporal derivatives. As a result, Eq. (3.1) and (3.2) become

$$\nabla\times\vec{E}\Big|_{t}=-\mu\frac{\vec{H}\Big|_{t+\Delta t/2}-\vec{H}\Big|_{t-\Delta t/2}}{\Delta t} \tag{3.3}$$

$$\nabla\times\vec{H}\Big|_{t+\Delta t/2}=\varepsilon\frac{\vec{E}\Big|_{t+\Delta t}-\vec{E}\Big|_{t}}{\Delta t} \tag{3.4}$$

where the subscript t and Δt denote time and the time step, respectively. Rearranging Eq. (3.3) and (3.4), we have

$$\vec{H}\Big|_{t+\Delta t/2}=\vec{H}\Big|_{t-\Delta t/2}-\frac{\Delta t}{\mu}\bullet(\nabla\times\vec{E}\Big|_{t}) \tag{3.5}$$

$$\vec{E}\Big|_{t+\Delta t}=\vec{E}\Big|_{t}+\frac{\Delta t}{\varepsilon}\bullet(\nabla\times\vec{H}\Big|_{t+\Delta t/2}) \tag{3.6}$$

Then, we expand the curl operator by the definition

$$\nabla\times\vec{E}=\begin{vmatrix}\hat{x} & \hat{y} & \hat{z}\\ \frac{\partial}{\partial x} & \frac{\partial}{\partial y} & \frac{\partial}{\partial z}\\ E_x & E_y & E_z\end{vmatrix}=(\frac{\partial E_z}{\partial y}-\frac{\partial E_y}{\partial z},\frac{\partial E_x}{\partial z}-\frac{\partial E_z}{\partial x},\frac{\partial E_y}{\partial x}-\frac{\partial E_x}{\partial y}) \tag{3.7}$$

$$\nabla\times\vec{H}=\begin{vmatrix}\hat{x} & \hat{y} & \hat{z}\\ \frac{\partial}{\partial x} & \frac{\partial}{\partial y} & \frac{\partial}{\partial z}\\ H_x & H_y & H_z\end{vmatrix}=(\frac{\partial H_z}{\partial y}-\frac{\partial H_y}{\partial z},\frac{\partial H_x}{\partial z}-\frac{\partial H_z}{\partial x},\frac{\partial H_y}{\partial x}-\frac{\partial H_x}{\partial y}) \tag{3.8}$$

with $\hat{u}$, E_u, and H_u representing respectively the unit vector, the scalar electric field, and the scalar magnetic field in the u direction, where $u\in\{x,y,z\}$.

Next, these derivatives in the curl operator can be evaluated by the Fourier transform. Since

$$g(x)=\sqrt{\frac{1}{2\pi}}\int_{-\infty}^{\infty}G(k)\times e^{ikx}dk \tag{3.9}$$

where $g(x)$ is an arbitrary function in the spatial domain (x space) and $G(k)$ denotes its Fourier transform in the spatial frequency domain (k space), the derivative of $g(x)$ can be computed as

$$\begin{aligned} \frac{d}{dx}g(x) &= \sqrt{\frac{1}{2\pi}}\frac{d}{dx}\int_{-\infty}^{\infty} G(k)\times e^{ikx}dk \\ &= \sqrt{\frac{1}{2\pi}}\int_{-\infty}^{\infty} ik\times G(k)\times e^{ikx}dk \\ &= F^{-1}\{ik\times F\{g(x)\}\} \end{aligned} \tag{3.10}$$

where i represents the imaginary unit $\sqrt{-1}$ as well as F and F^{-1} represent the Fourier transform and the inverse Fourier transform, respectively. By employing Eq. (3.10), the PSTD method calculates the spatial derivatives with the fast Fourier transform, an alternative to the Fourier transform in discrete space. Hence, Eq. (3.7) and (3.8) become

$$\begin{aligned} \nabla\times\vec{E} = (&IFFT_y\{ik_y\times FFT_y\{E_z\}\} - IFFT_z\{ik_z\times FFT_z\{E_y\}\}, \\ &IFFT_z\{ik_z\times FFT_z\{E_x\}\} - IFFT_x\{ik_x\times FFT_x\{E_z\}\}, \\ &IFFT_x\{ik_x\times FFT_x\{E_y\}\} - IFFT_y\{ik_y\times FFT_y\{E_x\}\}) \end{aligned} \tag{3.11}$$

$$\begin{aligned} \nabla\times\vec{H} = (&IFFT_y\{ik_y\times FFT_y\{H_z\}\} - IFFT_z\{ik_z\times FFT_z\{H_y\}\}, \\ &IFFT_z\{ik_z\times FFT_z\{H_x\}\} - IFFT_x\{ik_x\times FFT_x\{H_z\}\}, \\ &IFFT_x\{ik_x\times FFT_x\{H_y\}\} - IFFT_y\{ik_y\times FFT_y\{H_x\}\}) \end{aligned} \tag{3.12}$$

In Eq. (3.11) and (3.12), FFT_u, $IFFT_u$, and k_u respectively denote the fast Fourier transform, the inverse fast Fourier transform, and the spatial frequency in the u direction, where $u\in\{x,y,z\}$.

Finally, by plugging Eq. (3.11) and (3.12) into Eq. (3.5) and (3.6), respectively, we can have Eq. (3.13) ~ (3.18), which are the basic update equations of the PSTD algorithm.

doi:10.6342/NTU202501087

$$\vec{H}_x\Big|_{t+\Delta t/2} = \vec{H}_x\Big|_{t-\Delta t/2} - \frac{\Delta t}{\mu} \bullet (IFFT_y\{ik_y \times FFT_y\{E_z\big|_t\}\} - IFFT_z\{ik_z \times FFT_z\{E_y\big|_t\}\}) \tag{3.13}$$

$$\vec{H}_y\Big|_{t+\Delta t/2} = \vec{H}_y\Big|_{t-\Delta t/2} - \frac{\Delta t}{\mu} \bullet (IFFT_z\{ik_z \times FFT_z\{E_x\big|_t\}\} - IFFT_x\{ik_x \times FFT_x\{E_z\big|_t\}\}) \tag{3.14}$$

$$\vec{H}_z\Big|_{t+\Delta t/2} = \vec{H}_z\Big|_{t-\Delta t/2} - \frac{\Delta t}{\mu} \bullet (IFFT_x\{ik_x \times FFT_x\{E_y\big|_t\}\} - IFFT_y\{ik_y \times FFT_y\{E_x\big|_t\}\}) \tag{3.15}$$

$$\vec{E}_x\Big|_{t+\Delta t} = \vec{E}_x\Big|_t + \frac{\Delta t}{\varepsilon} \bullet (IFFT_y\{ik_y \times FFT_y\{H_z\big|_{t+\Delta t/2}\}\} - IFFT_z\{ik_z \times FFT_z\{H_y\big|_{t+\Delta t/2}\}\}) \tag{3.16}$$

$$\vec{E}_y\Big|_{t+\Delta t} = \vec{E}_y\Big|_t + \frac{\Delta t}{\varepsilon} \bullet (IFFT_z\{ik_z \times FFT_z\{H_x\big|_{t+\Delta t/2}\}\} - IFFT_x\{ik_x \times FFT_x\{H_z\big|_{t+\Delta t/2}\}\}) \tag{3.17}$$

$$\vec{E}_z\Big|_{t+\Delta t} = \vec{E}_z\Big|_t + \frac{\Delta t}{\varepsilon} \bullet (IFFT_x\{ik_x \times FFT_x\{H_y\big|_{t+\Delta t/2}\}\} - IFFT_y\{ik_y \times FFT_y\{H_x\big|_{t+\Delta t/2}\}\}) \tag{3.18}$$

Furthermore, in 2-D simulation space, the derivatives in the z direction are set to zero ($\partial / \partial z = 0$), which makes Eq. (3.13) ~ (3.18) deduce to

$$\vec{H}_x\Big|_{t+\Delta t/2} = \vec{H}_x\Big|_{t-\Delta t/2} - \frac{\Delta t}{\mu} \bullet (IFFT_y\{ik_y \times FFT_y\{E_z\big|_t\}\}) \tag{3.19}$$

$$\vec{H}_y\Big|_{t+\Delta t/2} = \vec{H}_y\Big|_{t-\Delta t/2} + \frac{\Delta t}{\mu} \bullet (IFFT_x\{ik_x \times FFT_x\{E_z\big|_t\}\}) \tag{3.20}$$

$$\vec{H}_z\Big|_{t+\Delta t/2} = \vec{H}_z\Big|_{t-\Delta t/2} - \frac{\Delta t}{\mu} \bullet (IFFT_x\{ik_x \times FFT_x\{E_y\big|_t\}\} - IFFT_y\{ik_y \times FFT_y\{E_x\big|_t\}\}) \tag{3.21}$$

$$\vec{E}_x\Big|_{t+\Delta t} = \vec{E}_x\Big|_t + \frac{\Delta t}{\varepsilon} \bullet (IFFT_y\{ik_y \times FFT_y\{H_z\big|_{t+\Delta t/2}\}\}) \tag{3.22}$$

$$\vec{E}_y\Big|_{t+\Delta t} = \vec{E}_y\Big|_t - \frac{\Delta t}{\varepsilon} \bullet (IFFT_x\{ik_x \times FFT_x\{H_z\big|_{t+\Delta t/2}\}\}) \tag{3.23}$$

$$\vec{E}_z\Big|_{t+\Delta t} = \vec{E}_z\Big|_t + \frac{\Delta t}{\varepsilon} \bullet (IFFT_x\{ik_x \times FFT_x\{H_y\big|_{t+\Delta t/2}\}\} - IFFT_y\{ik_y \times FFT_y\{H_x\big|_{t+\Delta t/2}\}\}) \tag{3.24}$$

Eq. (3.19), (3.20), and (3.24) only have the terms H_x, H_y, and E_z are called TM mode. Similarly, Eq. (3.21), (3.22), and (3.23) only have the terms E_x, E_y, and H_z are called TE mode. These equations form the fundamental PSTD algorithm in 2-D simulation space.

3.2 The Nyquist Sampling Theorem

The Nyquist sampling theorem defines the necessary sampling rate for a discrete signal to prevent aliasing distortion. As the PSTD method employs the fast Fourier transform for spatial discretization, the spatial sampling rate follows the Nyquist sampling theorem, making the PSTD method efficient in modeling large-scale problems. In this section, we introduce the Nyquist sampling theorem and highlight the reason why it allows efficient large-scale modeling.

Consider an arbitrary signal $g(x)$, whose Fourier transform is $G(k)$ with a finite bandwidth B. A series of sampling points with the spacing Δx is utilized to approximate $g(x)$. As a result, $g(x)$ is sampled at points $x_n = n\Delta x$ as

$$g_s(x) = g(x) \times \frac{1}{\Delta x} comb(\frac{x}{\Delta x}) = \sum_{n=-\infty}^{\infty} g(n\Delta x)\delta(x - n\Delta x) \tag{3.25}$$

where $g_s(x)$ is $g(x)$ with discrete samples, and $\delta(x)$ represents the Dirac delta function. By applying the convolution theorem, we calculate the Fourier transform of $g_s(x)$:

$$G_s(k) = G(k) * comb(\Delta x k) \tag{3.26}$$

where $G_s(k)$ is the Fourier transform of $g_s(x)$, and $*$ denotes the convolution. Observing Eq. (3.26), we can find that $G_s(k)$ reproduces itself with a period $1/\Delta x$, which is illustrated in Fig. 3.1. To prevent overlap between each duplicate, the period must satisfy

$$\frac{1}{\Delta x} \geq B \tag{3.27}$$

This crucial relation is known as the Nyquist sampling criterion, which states that the minimum sampling rate must be greater than or equal to the signal's bandwidth.

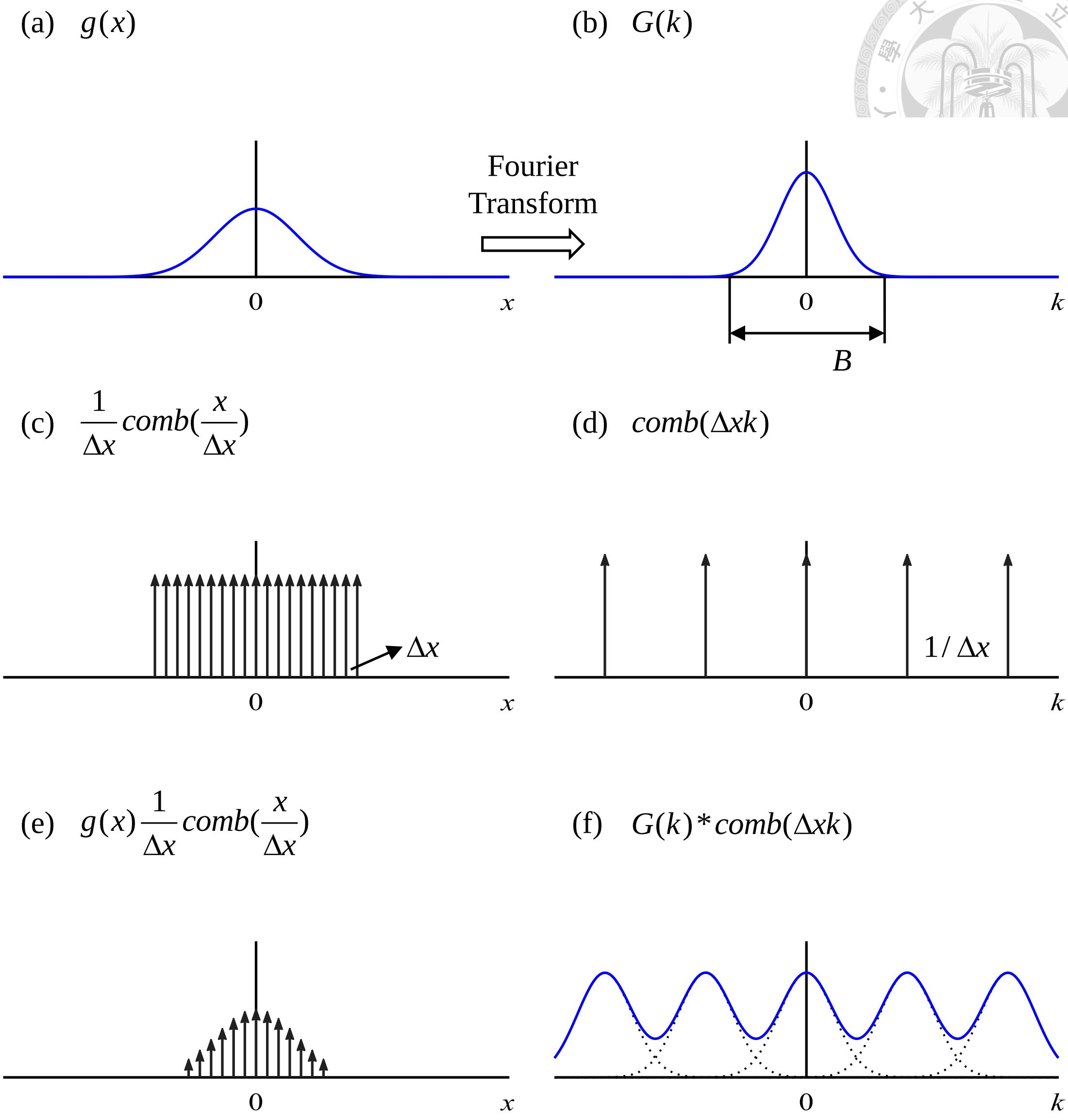

Fig. 3.1 A step-by-step demonstration of sampling a continuous signal into a discrete one in the spatial domain and its corresponding effect on the Fourier transform in the spatial frequency domain. (a) An arbitrary signal in the spatial domain. (b) The Fourier transform of (a), exhibiting a finite bandwidth B in the spatial frequency domain. (c) A series of Dirac delta functions spaced by Δx. Sampling a signal in the spatial domain with an interval Δx can be mathematically represented by multiplying it with (c). (d) The Fourier transform of (c). The series of Dirac delta functions is stretched in the frequency domain, resulting in a spacing of $1/\Delta x$. (e) The resulting discrete signal in the spatial domain after sampling. (f) The Fourier transform of (e). According to the convolution theorem, (b) is periodically replicated with a period $1/\Delta x$. To avoid overlap, the sampling rate $1/\Delta x$ must exceed the signal bandwidth B.

Consider a cosinusoidal signal $\cos(k_0 x)$ with a frequency k_0. Then, its Fourier transform is a set of two Dirac delta functions located at $-k_0$ and k_0, respectively. Therefore, the bandwidth B is $2k_0$, and Eq. (3.27) becomes

$$\frac{1}{\Delta x} \geq 2k_0 \tag{3.28}$$

This means that the sampling rate must be at least twice the oscillation frequency, ensuring there are sufficient data points to reconstruct the original signal. Specifically, sampling at least at the crest and trough of a single wavelength is required, as illustrated in Fig. 3.2.

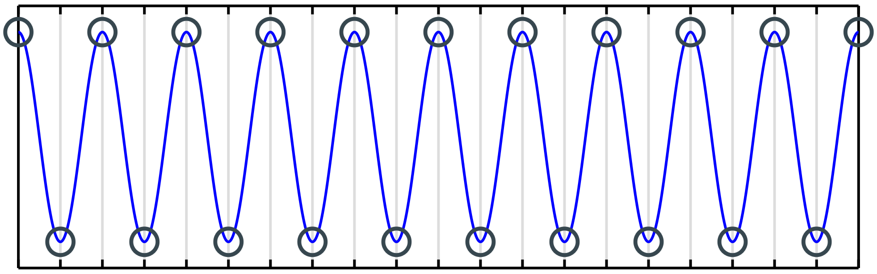

Fig. 3.2 Sampling a cosinusoidal signal at a sampling rate that is twice the frequency of the signal. In this scenario, the signal is sampled at the crest and trough, and there are just enough samples to perfectly reconstruct the original signal. This scenario is called the critical sampling scenario.

Once the Nyquist sampling criterion is not satisfied, the overlap between each duplicate occurs. Therefore, a set of frequencies $k_0 \pm n/\Delta x$ formed by a certain frequency k_0 plus or minus $1/\Delta x$ is not distinguishable. In other words, these frequencies all map onto the identical set of sampling points and thus cannot be differentiated based on the sampled data alone. Hence, when reconstructing the original signal from the sampling points, these frequencies are mixed, as illustrated in Fig. 3.3. This phenomenon is known as aliasing, and these frequencies are said to be aliased.

doi:10.6342/NTU202501087

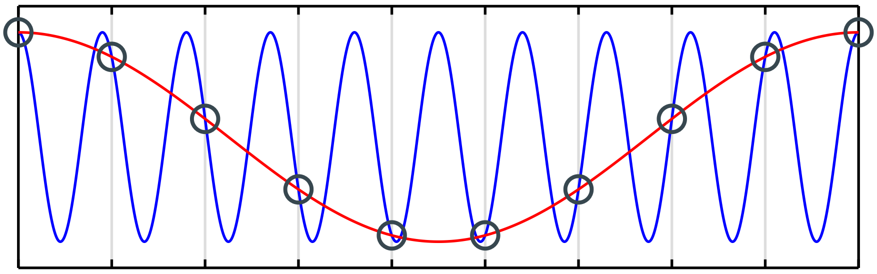

Fig. 3.3 Two different cosinusoidal signals that have the same sampling points. The two frequencies are aliased as the signal is reconstructed from the sampling points.

Based on the Nyquist sampling theorem, the PSTD method has a key advantage: it can achieve accuracy with just two spatial sampling points per wavelength. Compared to the FDTD method, which requires 20 spatial sampling points per wavelength, the PSTD method provides a coarser grid to save computational resources, especially in solving large-scale problems. Therefore, the PSTD method, with only two spatial samples per wavelength, efficiently models large-scale problems.

3.3 Numerical Dispersion and Stability

In this section, we introduce two key numerical factors that influence the accuracy of PSTD simulations: numerical dispersion and numerical stability. Both are affected by the choice of time step (temporal sampling rate). These topics are detailed in Sections 3.3.1 and 3.3.2, respectively.

3.3.1 Numerical Dispersion Relation

The dispersion relation describes the relationship between a wave's wave number and angular frequency. When we discretize the wave in both temporal and spatial domains, the time step affects the angular frequency, and the grid size influences the wave number.

doi:10.6342/NTU202501087

Hence, the dispersion relation must be modified to the numerical dispersion relation. The difference between these two relations yields errors called numerical dispersion, which causes inaccuracy in the wave. In this section, we present the numerical dispersion relation and see how the choice of time step affects it.

A harmonic plane wave can be written as

$$\vec{E}(x,y,z,t)=(E_x\hat{x}+E_y\hat{y}+E_z\hat{z})e^{-i(k_xx+k_yy+k_zz)}\times e^{i\omega t} \tag{3.29}$$

Here, ω is the angular frequency, and k_u is the wave number in the u direction, where $u\in\{x,y,z\}$. The plane wave satisfies the 3D wave equation:

$$\nabla^2\vec{E}-\frac{1}{c^2}\frac{\partial^2}{\partial t^2}\vec{E}=0 \tag{3.30}$$

By applying the vector calculus identity:

$$\nabla\times\nabla\times\vec{E}=\nabla(\nabla\bullet\vec{E})-\nabla^2\vec{E} \tag{3.31}$$

with $\nabla\bullet\vec{E}=0$ (source-free), Eq. (3.30) becomes

$$\frac{1}{c^2}\frac{\partial^2}{\partial t^2}\vec{E}=-\nabla\times\nabla\times\vec{E} \tag{3.32}$$

Considering a plane wave solution, the curl operator: $\nabla\times$ becomes $-i\vec{k}\times$ because

$$\begin{aligned}\nabla\times\vec{E}&=(\frac{\partial E_z}{\partial y}-\frac{\partial E_y}{\partial z},\frac{\partial E_x}{\partial z}-\frac{\partial E_z}{\partial x},\frac{\partial E_y}{\partial x}-\frac{\partial E_x}{\partial y})\\&=(-ik_yE_z-(-ik_zE_y),-ik_zE_x-(-ik_xE_z),-ik_xE_y-(-ik_yE_x))\\&=-i\vec{k}\times\vec{E}\end{aligned} \tag{3.33}$$

Hence, Eq. (3.32) becomes

$$\frac{1}{c^2}\frac{\partial^2}{\partial t^2}\vec{E}=\vec{k}\times\vec{k}\times\vec{E} \tag{3.34}$$

For the time derivative, the PSTD algorithm uses the central difference approximation:

$$\frac{d^2}{dt^2}f(u)=\frac{f(t+h)-2f(t)+f(t-h)}{h^2} \tag{3.35}$$

doi:10.6342/NTU202501087

where h represents the finite difference. Applying Eq. (3.35) to Eq. (3.34), the wave equation in the temporal discrete form is as follows:

$$\frac{\vec{E}\Big|_{\tau+1} - 2\vec{E}\Big|_{\tau} + \vec{E}\Big|_{\tau-1}}{c^2 \Delta t^2} = \vec{k} \times \vec{k} \times \vec{E}\Big|_{\tau} \tag{3.36}$$

The subscript τ denotes the τ-th time step in the temporal domain. Also, we can write Eq. (3.29) in the temporal discrete form:

$$\vec{E}\Big|_{\tau} = (E_x \hat{x} + E_y \hat{y} + E_z \hat{z}) e^{-i(k_x x + k_y y + k_z z)} \times e^{i\omega\tau\Delta t} \tag{3.37}$$

Plugging Eq. (3.37) into Eq. (3.36), we have

$$\frac{e^{i\omega\Delta t} - 2 + e^{-i\omega\Delta t}}{c^2 \Delta t^2} (E_x \hat{x} + E_y \hat{y} + E_z \hat{z}) = \vec{k} \times \vec{k} \times (E_x \hat{x} + E_y \hat{y} + E_z \hat{z}) \tag{3.38}$$

Recalling that

$$\sin(\theta) = \frac{e^{i\theta} - e^{-i\theta}}{2i} \Rightarrow \sin^2(\theta) = \frac{e^{i2\theta} - 2 + e^{-i2\theta}}{-4} \tag{3.39}$$

and expanding the cross product, Eq. (3.38) becomes

$$\frac{-4}{c^2 \Delta t^2} \sin^2(\frac{\omega \Delta t}{2}) E_x = k_x k_y E_y - {k_y}^2 E_x - {k_z}^2 E_x + k_x k_z E_z \tag{3.40}$$

$$\frac{-4}{c^2 \Delta t^2} \sin^2(\frac{\omega \Delta t}{2}) E_y = k_y k_z E_z - {k_z}^2 E_y - {k_x}^2 E_y + k_x k_y E_x \tag{3.41}$$

$$\frac{-4}{c^2 \Delta t^2} \sin^2(\frac{\omega \Delta t}{2}) E_z = k_x k_z E_x - {k_x}^2 E_z - {k_y}^2 E_z + k_y k_z E_y \tag{3.42}$$

Rewriting Eq. (3.40) ~ Eq. (3.42) into the matrix form, we have

$$\begin{pmatrix} -({k_y}^2 + {k_z}^2) & k_x k_y & k_x k_z \\ k_x k_y & -({k_x}^2 + {k_z}^2) & k_y k_z \\ k_x k_z & k_y k_z & -({k_x}^2 + {k_y}^2) \end{pmatrix} \begin{pmatrix} E_x \\ E_y \\ E_z \end{pmatrix} = \frac{-4}{c^2 \Delta t^2} \sin^2(\frac{\omega \Delta t}{2}) \begin{pmatrix} E_x \\ E_y \\ E_z \end{pmatrix} \tag{3.43}$$

Eq. (3.43) is an eigenvalue equation, so we determine the eigenvalues of the matrix by solving the characteristic equation. The eigenvalues, the corresponding eigenvectors, and their mode representations are listed in Table 3.1.

Table. 3.1 The eigenvalues of the matrix in Eq. (3.43), along with the corresponding eigenvectors and mode representations.

Eigenvalues	**Eigenvectors**	**Modes**
$-(k_x{}^2+k_y{}^2+k_z{}^2)=-k^2$	$\begin{pmatrix} \dfrac{-k_y}{k_x} & 1 & 0 \end{pmatrix}$	TE mode
$-(k_x{}^2+k_y{}^2+k_z{}^2)=-k^2$	$\begin{pmatrix} \dfrac{-k_z}{k_x} & 0 & 1 \end{pmatrix}$	TM mode
0	$\begin{pmatrix} \dfrac{k_x}{k_z} & \dfrac{k_y}{k_z} & 1 \end{pmatrix}$	Non-propagating mode

For TE and TM modes, setting the eigenvalues in Table 3.1 and Eq. (3.43) are equal, we get the numerical dispersion relation:

$$k=\frac{2}{c\Delta t}\sin(\frac{\omega\Delta t}{2}) \tag{3.44}$$

Based on the Nyquist sampling theorem, the fast Fourier transform algorithm gives an exact representation for $|k_u| \le \pi/\Delta u$. Here, Δu is the cell size in the u direction, where $u \in \{x, y, z\}$. For an infinitesimal time step, $\sin(\omega\Delta t/2) \approx \omega\Delta t/2$, and Eq. (3.44) reduces to

$$k=\frac{\omega}{c} \tag{3.45}$$

which is the exact dispersion relation. Comparing Eq. (3.44) with Eq. (3.45), we find that discretizing the wave equation in the temporal and spatial domains makes the dispersion relation dependent on the time step. Hence, the choice of the time step alters the numerical dispersion relation and influences the numerical dispersion errors, affecting the accuracy of PSTD simulations.

3.3.2 The Courant Stability Condition

Discretization in the spatial and temporal domains introduces truncation errors in a PSTD simulation. While these errors are initially negligible, they accumulate over time and can become comparable in magnitude to the simulated values, leading to numerical instability. Hence, the choice of time step directly affects the time evolution of the PSTD simulation, which in turn influences its numerical stability and ultimately determines its overall accuracy. To ensure stability and prevent error growth, the time step must satisfy a specific condition known as the Courant stability condition, which is derived in this section.

We start from the numerical dispersion relation (Eq. (3.44)) and solve for ω, which gives

$$\omega = \frac{2}{\Delta t}\arcsin\left(\frac{kc\Delta t}{2}\right) \tag{3.46}$$

Recall that Eq. (3.37) gives the discrete plane wave solution. As a result, the imaginary value of ω causes a decay of the plane wave, leading to an unstable wave solution. Therefore, the value in the arcsin function in Eq. (3.46) must be constrained to yield real values. In other words,

$$0 < \frac{kc\Delta t}{2} \leq 1 \tag{3.47}$$

Eq. (3.47) must be fulfilled in the worst-case scenario, where

$$k_{\max} = 2\pi\sqrt{\left(\frac{1}{2\Delta x}\right)^2 + \left(\frac{1}{2\Delta y}\right)^2 + \left(\frac{1}{2\Delta z}\right)^2} \tag{3.48}$$

which is based on the Nyquist sampling theorem. Substituting Eq. (3.48) into Eq. (3.47), we have

$$\Delta t \leq \frac{1}{\pi c\sqrt{\left(\frac{1}{2\Delta x}\right)^2 + \left(\frac{1}{2\Delta y}\right)^2 + \left(\frac{1}{2\Delta z}\right)^2}} \tag{3.49}$$

doi:10.6342/NTU202501087

Eq. (3.49) is known as the Courant-Friedrich-Levy (CFL) or Courant stability condition. Furthermore, in the 1-D case ($\Delta x = \Delta y = \infty$), Eq. (3.49) deduces to

$$\Delta t \le \frac{2\Delta z}{\pi c} \Leftrightarrow \frac{c\Delta t}{\Delta z} \le \frac{2}{\pi} \tag{3.50}$$

In the 2-D case ($\Delta z = \infty$), with $\Delta x = \Delta y = \Delta$, Eq. (3.49) deduces to

$$\Delta t \le \frac{\sqrt{2}\Delta}{\pi c} \Leftrightarrow \frac{c\Delta t}{\Delta} \le \frac{\sqrt{2}}{\pi} \tag{3.51}$$

In the 3-D case, with $\Delta x = \Delta y = \Delta z = \Delta$, Eq. (3.49) deduces to

$$\Delta t \le \frac{2\Delta}{\sqrt{3}\pi c} \Leftrightarrow \frac{c\Delta t}{\Delta} \le \frac{2}{\sqrt{3}\pi} \tag{3.52}$$

As the Nyquist sampling theorem determines the grid size, these conditions determine the critical time steps that produce stable results in 1-D, 2-D, and 3-D PSTD simulations.

3.4 Simple Soft Source

A simple soft source is preferable in PSTD simulations due to its non-reflecting nature. Eq. (3.53) presents the scheme of implementing a simple soft source in PSTD simulations:

$$E\Big|_{\tau}^{i_{src}} = E\Big|_{\tau}^{i_{src}} + f_{src}(t)\Big|_{\tau} \tag{3.53}$$

where the subscript τ denotes the τ-th time step in the temporal domain, the superscript i_{src} denotes the source grid point, and the function $f_{src}(t)$ is the temporal function that represents a designed source. At the source grid point, incorporating the source by adding field values (a soft source) instead of assigning field values (a hard source) avoids the erasure of scattered waves, which causes the reflection of electromagnetic waves. As a result, a simple soft source prevents scattered waves from reflection and is preferred in PSTD simulations.

doi:10.6342/NTU202501087

Although the PSTD method is computationally efficient, it is problematic for implementing a simple soft source. Performing differentiation by the fast Fourier transform reduces computational resource consumption; however, because of the Gibbs phenomenon, the fast Fourier transform makes the PSTD method vulnerable to discontinuities. Unfortunately, discontinuities definitely occur when introducing sources, which creates unwanted errors in PSTD simulations. Therefore, researchers have come up with alternative approaches that can effectively resolve this issue.

In 2004, Tae-Woo Lee and Susan C. Hagness demonstrated that a compact wave source condition can minimize the errors caused by the Gibbs phenomenon when incorporating a simple soft source in PSTD simulations [32]. In the following, we briefly review this approach and explain the reasoning behind its ability to mitigate source-induced errors in PSTD simulations.

Consider two 1-D PSTD simulations with 120 spatial grids and the corresponding grid index i, ranging from 1 to 120. In the first simulation, we employ a simple soft source at the simulation grid center ($i = 60$). The temporal source function in this simulation, represented by $f(t)$, is chosen as a cosinusoidal function. In the second simulation, we divide the source into two identical segments ($f_1(t) = f_2(t) = f(t)/2$) and implement them at two adjacent grid points ($i = 60$ and $i = 61$). The first and second simulations are called single and twin source conditions.

Here, we depict early-time electric field distributions across the 1-D simulation grid with both source conditions in Fig. 3.4. As illustrated in Fig. 3.4 (a), the single source scenario shows a notable limitation, highlighted by the oscillations on both sides that indicate the Gibbs phenomenon. On the other hand, Fig. 3.4 (b) demonstrates that the twin source condition effectively decreases the Gibbs phenomenon, leading to a flat result on both sides.

doi:10.6342/NTU202501087

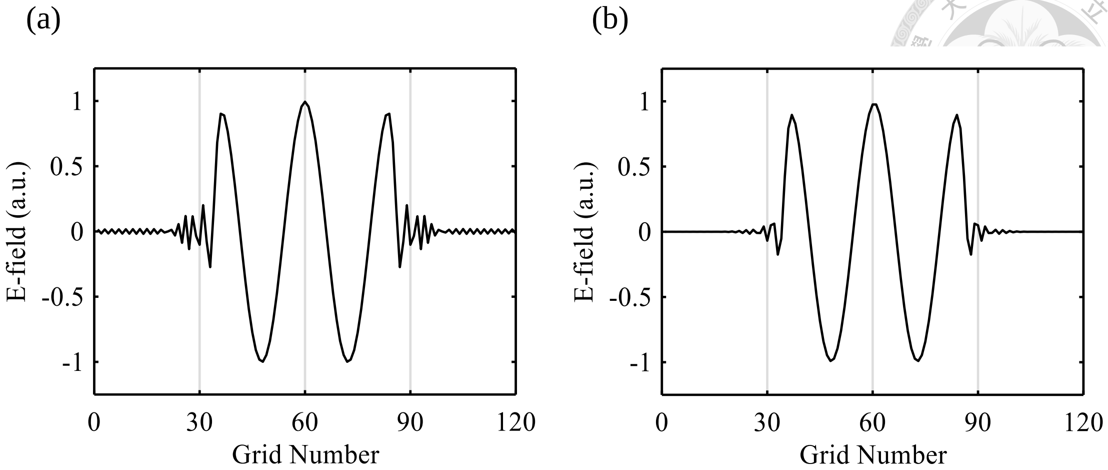

Fig. 3.4 Early-time snapshots of electric field distribution in a 1-D simulation grid. A cosinusoidal simple soft source is excited at the grid center by (a) the single source condition situated at $i = 60$ and (b) the twin source condition situated at $i = 60$ and $i = 61$. Comparing (a) with (b), the twin source condition lowers the impact of the Gibbs phenomenon, making PSTD simulations errorless when introducing a simple soft source.

The reasoning behind the alleviation of the Gibbs phenomenon by the twin source condition is explained in Fig. 3.5. In the twin source scenario, the source $f(t)$ is generated by the superposition of two identical half single sources ($f_1(t) = f_2(t) = f(t)/2$) separated by one grid point ($i = 60$ and $i = 61$). In Fig. 3.5, the electric field distribution created by the twin source condition is represented by a black solid line, while the electric field distributions from the half single sources located at $i = 60$ and $i = 61$ are shown as blue and red dashed lines, respectively. Observing Fig. 3.5, we find that although each of the two half single sources individually exhibits the Gibbs phenomenon, their compact superposition effectively cancels out the resulting ripples. In this sense, the twin source condition does not suppress the Gibbs phenomenon but shifts it to achieve self-cancellation. This explains why the twin source condition successfully mitigates the Gibbs phenomenon, making it an errorless source implementation.

doi:10.6342/NTU202501087

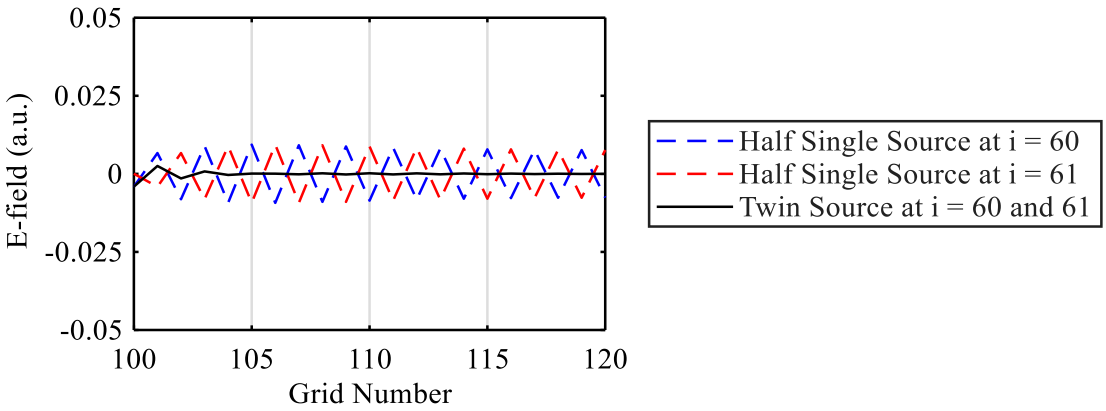

Fig. 3.5 Early-time snapshots of electric field distribution in a 1-D simulation grid from 100 to 120 with the half single source located at $i = 60$, the half single source located at $i = 61$, and a twin source condition located at $i = 60$ and 61. The mutual cancellation of two oscillations created by the two single sources makes the twin source condition exhibit no Gibbs phenomenon, leading to a smoother electric field distribution profile.

3.5 Perfectly Matched Layer Absorbing Boundary Conditions

The PML is an absorbing boundary condition used to minimize numerical reflections from the boundaries of a truncated computational domain. In numerical simulations, artificial reflections occur at boundaries due to the abrupt change in material properties, ruining the computational results in the problem space. However, with a PML, outgoing waves are absorbed on the boundaries and no longer interact with the waves in the simulation domain. Therefore, we can simulate an infinite space within a finite computational domain.

In 1994, Jean-Pierre Berenger first introduced the PML [33]. He split field components into two distinct parts and incorporated conductivities to create a non-physical anisotropic medium that attenuates wave intensity and eliminates reflections. Since then, researchers have explored PMLs through various approaches, including uniaxial PML, stretched-coordinate PML, and convolutional PML.

The key concept of the PML is introducing conductivity to attenuate wave propagation and matching the impedance of a PML and non-PML region to prevent reflections. In the following, we use the PML approach proposed by Zachary S. Sacks for further explanations [34]. Finally, we formulate the PSTD update equations with the PML.

Consider a non-PML region that has a relative permeability tensor $[\mu_r]$ and permittivity tensor $[\varepsilon_r]$. We first consider wave propagation in the z direction. To ensure that the impedance of a PML region and the non-PML region are matched, the relative permeability tensor and permittivity tensor of the PML region are respectively chosen as $[\mu_r][S_z]$ and $[\varepsilon_r][S_z]$, where

$$[S_z]=\begin{pmatrix} a & 0 & 0 \\ 0 & b & 0 \\ 0 & 0 & c \end{pmatrix} \tag{3.54}$$

Also, Snell's law for incidence to a diagonally anisotropic medium is:

$$\sin\theta_1=\sqrt{bc}\sin\theta_2 \tag{3.55}$$

and the Fresnel equations for incidence on a diagonally anisotropic medium are:

$$r_{TE}=\frac{\sqrt{a}\cos\theta_1-\sqrt{b}\cos\theta_2}{\sqrt{a}\cos\theta_1+\sqrt{b}\cos\theta_2} \tag{3.56}$$

$$r_{TM}=\frac{-\sqrt{a}\cos\theta_1+\sqrt{b}\cos\theta_2}{\sqrt{a}\cos\theta_1+\sqrt{b}\cos\theta_2} \tag{3.57}$$

where θ_1 and θ_2 are incident and refraction angles, respectively. We choose $bc=1$ so that no refraction occurs ($\theta_1=\theta_2$). Hence, Eq. (3.56) and (3.57) reduce to

$$r_{TE}=\frac{\sqrt{a}-\sqrt{b}}{\sqrt{a}+\sqrt{b}} \tag{3.58}$$

$$r_{TM}=\frac{-\sqrt{a}+\sqrt{b}}{\sqrt{a}+\sqrt{b}} \tag{3.59}$$

doi:10.6342/NTU202501087

We further choose $a = b$ so that there is no reflection regardless of the angle of incidence and polarization. Therefore, we rewrite

$$[S_z] = \begin{pmatrix} s_z & 0 & 0 \\ 0 & s_z & 0 \\ 0 & 0 & s_z^{-1} \end{pmatrix} \tag{3.60}$$

Following the same process, we can write

$$[S_x] = \begin{pmatrix} s_x^{-1} & 0 & 0 \\ 0 & s_x & 0 \\ 0 & 0 & s_x \end{pmatrix} \tag{3.61}$$

$$[S_y] = \begin{pmatrix} s_y & 0 & 0 \\ 0 & s_y^{-1} & 0 \\ 0 & 0 & s_y \end{pmatrix} \tag{3.62}$$

Next, the PML should be employed in 3 dimensions so the relative permeability tensor and permittivity tensor are respectively chosen as $[\mu_r][S]$ and $[\varepsilon_r][S]$, where

$$[S] = [S_x][S_y][S_z] = \begin{pmatrix} \dfrac{s_y s_z}{s_x} & 0 & 0 \\ 0 & \dfrac{s_x s_z}{s_y} & 0 \\ 0 & 0 & \dfrac{s_x s_y}{s_z} \end{pmatrix} \tag{3.63}$$

Finally, to attenuate waves in the PML region, we introduce conductivities by selecting

$$s_x = 1 + \frac{\sigma_x'}{i\omega\varepsilon_0} \tag{3.64}$$

$$s_y = 1 + \frac{\sigma_y'}{i\omega\varepsilon_0} \tag{3.65}$$

$$s_z = 1 + \frac{\sigma_z'}{i\omega\varepsilon_0} \tag{3.66}$$

with σ_u' the artificial conductivity in the u direction, where $u \in \{x, y, z\}$.

doi:10.6342/NTU202501087

Hence, the two Maxwell's equations, incorporated with the PML (ignoring material conductivities) in the frequency domain, become

$$\nabla\times\vec{E}(\omega)=-i\omega\mu_0[\mu_r][S]\vec{H}(\omega) \tag{3.67}$$

$$\nabla\times\vec{H}(\omega)=i\omega[S]\vec{D}(\omega) \tag{3.68}$$

with the electric field constitutive relation:

$$\vec{D}(\omega)=\varepsilon_0[\varepsilon_r]\vec{E}(\omega) \tag{3.69}$$

Expanding the curl operators and the tensors, we have

$$i\omega(1+\frac{\sigma'_x}{i\omega\varepsilon_0})^{-1}(1+\frac{\sigma'_y}{i\omega\varepsilon_0})(1+\frac{\sigma'_z}{i\omega\varepsilon_0})H_x(\omega)=-\frac{1}{\mu_0\mu_{xx}}\left(\frac{\partial E_z(\omega)}{\partial y}-\frac{\partial E_y(\omega)}{\partial z}\right) \tag{3.70}$$

$$i\omega(1+\frac{\sigma'_x}{i\omega\varepsilon_0})(1+\frac{\sigma'_y}{i\omega\varepsilon_0})^{-1}(1+\frac{\sigma'_z}{i\omega\varepsilon_0})H_y(\omega)=-\frac{1}{\mu_0\mu_{yy}}\left(\frac{\partial E_x(\omega)}{\partial z}-\frac{\partial E_z(\omega)}{\partial x}\right) \tag{3.71}$$

$$i\omega(1+\frac{\sigma'_x}{i\omega\varepsilon_0})(1+\frac{\sigma'_y}{i\omega\varepsilon_0})(1+\frac{\sigma'_z}{i\omega\varepsilon_0})^{-1}H_z(\omega)=-\frac{1}{\mu_0\mu_{zz}}\left(\frac{\partial E_y(\omega)}{\partial x}-\frac{\partial E_x(\omega)}{\partial y}\right) \tag{3.72}$$

$$i\omega(1+\frac{\sigma'_x}{i\omega\varepsilon_0})^{-1}(1+\frac{\sigma'_y}{i\omega\varepsilon_0})(1+\frac{\sigma'_z}{i\omega\varepsilon_0})D_x(\omega)=\left(\frac{\partial H_z(\omega)}{\partial y}-\frac{\partial H_y(\omega)}{\partial z}\right) \tag{3.73}$$

$$i\omega(1+\frac{\sigma'_x}{i\omega\varepsilon_0})(1+\frac{\sigma'_y}{i\omega\varepsilon_0})^{-1}(1+\frac{\sigma'_z}{i\omega\varepsilon_0})D_y(\omega)=\left(\frac{\partial H_x(\omega)}{\partial z}-\frac{\partial H_z(\omega)}{\partial x}\right) \tag{3.74}$$

$$i\omega(1+\frac{\sigma'_x}{i\omega\varepsilon_0})(1+\frac{\sigma'_y}{i\omega\varepsilon_0})(1+\frac{\sigma'_z}{i\omega\varepsilon_0})^{-1}D_z(\omega)=\left(\frac{\partial H_y(\omega)}{\partial x}-\frac{\partial H_x(\omega)}{\partial y}\right) \tag{3.75}$$

$$D_x(\omega)=\varepsilon_0\varepsilon_{xx}E_x(\omega) \tag{3.76}$$

$$D_y(\omega)=\varepsilon_0\varepsilon_{yy}E_y(\omega) \tag{3.77}$$

$$D_z(\omega)=\varepsilon_0\varepsilon_{zz}E_z(\omega) \tag{3.78}$$

doi:10.6342/NTU202501087

Then, we use the Fourier transform properties listed in Eq. (3.79) to convert Eq. (3.70) ~ (3.78) to the temporal domain.

$$\begin{aligned} &1.\ F\left\{g(t)\right\}=G(\omega) && 2.\ F\left\{\frac{d^n}{dt^n}g(t)\right\}=(i\omega)^n G(\omega) \\ &3.\ F\left\{ag(t)\right\}=aG(\omega) && 4.\ F\left\{\int_{-\infty}^{t} g(\tau)d\tau\right\}=\frac{1}{i\omega}G(\omega) \end{aligned} \tag{3.79}$$

Hence, Eq. (3.70) ~ (3.78) become

$$\frac{\partial}{\partial t}H_x(t)+\frac{\sigma_y'+\sigma_z'}{\varepsilon_0}H_x(t)+\frac{\sigma_y'\sigma_z'}{{\varepsilon_0}^2}\int_{-\infty}^{t}H_x(\tau)d\tau=-\frac{1}{\mu_0\mu_{xx}}C_x^E(t)-\frac{\sigma_x'}{\mu_0\mu_{xx}\varepsilon_0}\int_{-\infty}^{t}C_x^E(\tau)d\tau \tag{3.80}$$

$$\frac{\partial}{\partial t}H_y(t)+\frac{\sigma_x'+\sigma_z'}{\varepsilon_0}H_y(t)+\frac{\sigma_x'\sigma_z'}{{\varepsilon_0}^2}\int_{-\infty}^{t}H_y(\tau)d\tau=-\frac{1}{\mu_0\mu_{yy}}C_y^E(t)-\frac{\sigma_y'}{\mu_0\mu_{yy}\varepsilon_0}\int_{-\infty}^{t}C_y^E(\tau)d\tau \tag{3.81}$$

$$\frac{\partial}{\partial t}H_z(t)+\frac{\sigma_x'+\sigma_y'}{\varepsilon_0}H_z(t)+\frac{\sigma_x'\sigma_y'}{{\varepsilon_0}^2}\int_{-\infty}^{t}H_z(\tau)d\tau=-\frac{1}{\mu_0\mu_{zz}}C_z^E(t)-\frac{\sigma_z'}{\mu_0\mu_{zz}\varepsilon_0}\int_{-\infty}^{t}C_z^E(\tau)d\tau \tag{3.82}$$

$$\frac{\partial}{\partial t}D_x(t)+\frac{\sigma_y'+\sigma_z'}{\varepsilon_0}D_x(t)+\frac{\sigma_y'\sigma_z'}{{\varepsilon_0}^2}\int_{-\infty}^{t}D_x(\tau)d\tau=C_x^H(t)+\frac{\sigma_x'}{\varepsilon_0}\int_{-\infty}^{t}C_x^H(\tau)d\tau \tag{3.83}$$

$$\frac{\partial}{\partial t}D_y(t)+\frac{\sigma_x'+\sigma_z'}{\varepsilon_0}D_y(t)+\frac{\sigma_x'\sigma_z'}{{\varepsilon_0}^2}\int_{-\infty}^{t}D_y(\tau)d\tau=C_y^H(t)+\frac{\sigma_y'}{\varepsilon_0}\int_{-\infty}^{t}C_y^H(\tau)d\tau \tag{3.84}$$

$$\frac{\partial}{\partial t}D_z(t)+\frac{\sigma_x'+\sigma_y'}{\varepsilon_0}D_z(t)+\frac{\sigma_x'\sigma_y'}{{\varepsilon_0}^2}\int_{-\infty}^{t}D_z(\tau)d\tau=C_z^H(t)+\frac{\sigma_z'}{\varepsilon_0}\int_{-\infty}^{t}C_z^H(\tau)d\tau \tag{3.85}$$

$$D_x(t)=\varepsilon_0\varepsilon_{xx}E_x(t) \tag{3.86}$$

$$D_y(t)=\varepsilon_0\varepsilon_{yy}E_y(t) \tag{3.87}$$

$$D_z(t)=\varepsilon_0\varepsilon_{zz}E_z(t) \tag{3.88}$$

where

$$\begin{aligned} &C_x^E(t)=\frac{\partial E_z(\omega)}{\partial y}-\frac{\partial E_y(\omega)}{\partial z},\ C_y^E(t)=\frac{\partial E_x(\omega)}{\partial z}-\frac{\partial E_z(\omega)}{\partial x},\ C_z^E(t)=\frac{\partial E_y(\omega)}{\partial x}-\frac{\partial E_x(\omega)}{\partial y} \\ &C_x^H(t)=\frac{\partial H_z(\omega)}{\partial y}-\frac{\partial H_y(\omega)}{\partial z},\ C_y^H(t)=\frac{\partial H_x(\omega)}{\partial z}-\frac{\partial H_z(\omega)}{\partial x},\ C_z^H(t)=\frac{\partial H_y(\omega)}{\partial x}-\frac{\partial H_x(\omega)}{\partial y} \end{aligned} \tag{3.89}$$

Next, in discretization, we use the central difference approximation for the temporal derivatives and the fast Fourier transform for the spatial derivatives. Also, time integrals are replaced with summations. Hence, Eq. (3.80) ~ (3.88) become

$$\begin{aligned}&\frac{H_x|_{t+\Delta t/2}-H_x|_{t-\Delta t/2}}{\Delta t}+\frac{\sigma'_y+\sigma'_z}{\varepsilon_0}\left(\frac{H_x|_{t+\Delta t/2}+H_x|_{t-\Delta t/2}}{2}\right)\\&+\frac{\sigma'_y\sigma'_z\Delta t}{{\varepsilon_0}^2}\left[\frac{1}{4}\left(\frac{H_x|_{t+\Delta t/2}+H_x|_{t-\Delta t/2}}{2}\right)+I_{Hx}|_{t-\Delta t/2}\right]=-\frac{1}{\mu_0\mu_{xx}}C_x^E\Big|_t-\frac{\Delta t\sigma'_x}{\mu_0\mu_{xx}\varepsilon_0}I_{CEx}|_t\end{aligned}\tag{3.90}$$

$$\begin{aligned}&\frac{H_y|_{t+\Delta t/2}-H_y|_{t-\Delta t/2}}{\Delta t}+\frac{\sigma'_x+\sigma'_z}{\varepsilon_0}\left(\frac{H_y|_{t+\Delta t/2}+H_y|_{t-\Delta t/2}}{2}\right)\\&+\frac{\sigma'_x\sigma'_z\Delta t}{{\varepsilon_0}^2}\left[\frac{1}{4}\left(\frac{H_y|_{t+\Delta t/2}+H_y|_{t-\Delta t/2}}{2}\right)+I_{Hy}|_{t-\Delta t/2}\right]=-\frac{1}{\mu_0\mu_{yy}}C_y^E\Big|_t-\frac{\Delta t\sigma'_y}{\mu_0\mu_{yy}\varepsilon_0}I_{CEy}|_t\end{aligned}\tag{3.91}$$

$$\begin{aligned}&\frac{H_z|_{t+\Delta t/2}-H_z|_{t-\Delta t/2}}{\Delta t}+\frac{\sigma'_x+\sigma'_y}{\varepsilon_0}\left(\frac{H_z|_{t+\Delta t/2}+H_z|_{t-\Delta t/2}}{2}\right)\\&+\frac{\sigma'_x\sigma'_y\Delta t}{{\varepsilon_0}^2}\left[\frac{1}{4}\left(\frac{H_z|_{t+\Delta t/2}+H_z|_{t-\Delta t/2}}{2}\right)+I_{Hz}|_{t-\Delta t/2}\right]=-\frac{1}{\mu_0\mu_{zz}}C_z^E\Big|_t-\frac{\Delta t\sigma'_z}{\mu_0\mu_{zz}\varepsilon_0}I_{CEz}|_t\end{aligned}\tag{3.92}$$

$$\begin{aligned}&\frac{D_x|_{t+\Delta t}-D_x|_t}{\Delta t}+\frac{\sigma'_y+\sigma'_z}{\varepsilon_0}\left(\frac{D_x|_{t+\Delta t}+D_x|_t}{2}\right)\\&+\frac{\sigma'_y\sigma'_z\Delta t}{{\varepsilon_0}^2}\left[\frac{1}{4}\left(\frac{D_x|_{t+\Delta t}+D_x|_t}{2}\right)+I_{Dx}|_t\right]=C_x^H\Big|_t+\frac{\Delta t\sigma'_x}{\varepsilon_0}I_{CHx}|_{t+\Delta t/2}\end{aligned}\tag{3.93}$$

$$\begin{aligned}&\frac{D_y|_{t+\Delta t}-D_y|_t}{\Delta t}+\frac{\sigma'_x+\sigma'_z}{\varepsilon_0}\left(\frac{D_y|_{t+\Delta t}+D_y|_t}{2}\right)\\&+\frac{\sigma'_x\sigma'_z\Delta t}{{\varepsilon_0}^2}\left[\frac{1}{4}\left(\frac{D_y|_{t+\Delta t}+D_y|_t}{2}\right)+I_{Dy}|_t\right]=C_y^H\Big|_t+\frac{\Delta t\sigma'_y}{\varepsilon_0}I_{CHy}|_{t+\Delta t/2}\end{aligned}\tag{3.94}$$

$$\begin{aligned}&\frac{D_z|_{t+\Delta t}-D_z|_t}{\Delta t}+\frac{\sigma'_x+\sigma'_y}{\varepsilon_0}\left(\frac{D_z|_{t+\Delta t}+D_z|_t}{2}\right)\\&+\frac{\sigma'_x\sigma'_y\Delta t}{{\varepsilon_0}^2}\left[\frac{1}{4}\left(\frac{D_z|_{t+\Delta t}+D_z|_t}{2}\right)+I_{Dz}|_t\right]=C_z^H\Big|_t+\frac{\Delta t\sigma'_z}{\varepsilon_0}I_{CHz}|_{t+\Delta t/2}\end{aligned}\tag{3.95}$$

$$D_x\big|_{t+\Delta t} = \varepsilon_0 \varepsilon_{xx}\, E_x\big|_{t+\Delta t} \tag{3.96}$$

$$D_y\big|_{t+\Delta t} = \varepsilon_0 \varepsilon_{yy}\, E_y\big|_{t+\Delta t} \tag{3.97}$$

$$D_z\big|_{t+\Delta t} = \varepsilon_0 \varepsilon_{zz}\, E_z\big|_{t+\Delta t} \tag{3.98}$$

Here,

$$\begin{aligned}
C_x^E\big|_t &= IFFT_y\{ik_y \times FFT_y\{E_z\big|_t\}\} - IFFT_z\{ik_z \times FFT_z\{E_y\big|_t\}\} \\
C_y^E\big|_t &= IFFT_z\{ik_z \times FFT_z\{E_x\big|_t\}\} - IFFT_x\{ik_x \times FFT_x\{E_z\big|_t\}\} \\
C_z^E\big|_t &= IFFT_x\{ik_x \times FFT_x\{E_y\big|_t\}\} - IFFT_y\{ik_y \times FFT_y\{E_x\big|_t\}\} \\
C_x^H\big|_t &= IFFT_y\{ik_y \times FFT_y\{H_z\big|_{t+\Delta t/2}\}\} - IFFT_z\{ik_z \times FFT_z\{H_y\big|_{t+\Delta t/2}\}\} \\
C_y^H\big|_t &= IFFT_z\{ik_z \times FFT_z\{H_x\big|_{t+\Delta t/2}\}\} - IFFT_x\{ik_x \times FFT_x\{H_z\big|_{t+\Delta t/2}\}\} \\
C_z^H\big|_t &= IFFT_x\{ik_x \times FFT_x\{H_y\big|_{t+\Delta t/2}\}\} - IFFT_y\{ik_y \times FFT_y\{H_x\big|_{t+\Delta t/2}\}\}
\end{aligned} \tag{3.99}$$

$$\begin{aligned}
I_{Hu}\big|_{t-\Delta t/2} &= \sum_{T=\Delta t/2}^{t-\Delta t/2} H_u\big|_T \qquad & I_{CEu}\big|_t &= \sum_{T=0}^{t} C_u^E\big|_T \\
I_{Du}\big|_t &= \sum_{T=0}^{t} D_u\big|_T \qquad & I_{CHu}\big|_{t+\Delta t/2} &= \sum_{T=\Delta t/2}^{t+\Delta t/2} C_u^H\big|_T
\end{aligned} \tag{3.100}$$

where $u \in \{x, y, z\}$. Finally, we collect the same terms and rearrange the equations to build the update equations:

$$H_x\big|_{t+\Delta t/2} = m_{Hx1}\, H_x\big|_{t-\Delta t/2} + m_{Hx2}\, C_x^E\big|_t + m_{Hx3}\, I_{CEx}\big|_t + m_{Hx4}\, I_{Hx}\big|_{t-\Delta t/2} \tag{3.101}$$

$$H_y\big|_{t+\Delta t/2} = m_{Hy1}\, H_y\big|_{t-\Delta t/2} + m_{Hy2}\, C_y^E\big|_t + m_{Hy3}\, I_{CEy}\big|_t + m_{Hy4}\, I_{Hy}\big|_{t-\Delta t/2} \tag{3.102}$$

$$H_z\big|_{t+\Delta t/2} = m_{Hz1}\, H_z\big|_{t-\Delta t/2} + m_{Hz2}\, C_z^E\big|_t + m_{Hz3}\, I_{CEz}\big|_t + m_{Hz4}\, I_{Hz}\big|_{t-\Delta t/2} \tag{3.103}$$

$$D_x\big|_{t+\Delta t} = m_{Dx1}\, D_x\big|_t + m_{Dx2}\, C_x^H\big|_{t+\Delta t/2} + m_{Dx3}\, I_{CHx}\big|_{t+\Delta t/2} + m_{Dx4}\, I_{Dx}\big|_t \tag{3.104}$$

$$D_y\big|_{t+\Delta t} = m_{Dy1}\, D_y\big|_t + m_{Dy2}\, C_y^H\big|_{t+\Delta t/2} + m_{Dy3}\, I_{CHy}\big|_{t+\Delta t/2} + m_{Dy4}\, I_{Dy}\big|_t \tag{3.105}$$

$$D_z\big|_{t+\Delta t} = m_{Dz1}\, D_z\big|_t + m_{Dz2}\, C_z^H\big|_{t+\Delta t/2} + m_{Dz3}\, I_{CHz}\big|_{t+\Delta t/2} + m_{Dz4}\, I_{Dz}\big|_t \tag{3.106}$$

where the coefficients of each term are listed in Eq. (3.107) ~ (3.109), along with the three electric field constitutive relations listed in Eq. (3.110) ~ (3.112).

$$\begin{aligned}
&m_{Hx0}=m_{Dx0}=\frac{1}{\Delta t}+\frac{\sigma_y'+\sigma_z'}{2\varepsilon_0}+\frac{\sigma_y'\sigma_z'\Delta t}{4{\varepsilon_0}^2}\\
&m_{Hx1}=m_{Dx1}=\frac{1}{m_{Hx0}}(\frac{1}{\Delta t}-\frac{\sigma_y'+\sigma_z'}{2\varepsilon_0}-\frac{\sigma_y'\sigma_z'\Delta t}{4{\varepsilon_0}^2})\\
&m_{Hx2}=-\frac{1}{m_{Hx0}}\frac{1}{\mu_0\mu_{xx}},\ m_{Dx2}=\frac{1}{m_{Dx0}}\\
&m_{Hx3}=-\frac{1}{m_{Hx0}}\frac{\Delta t\sigma_x'}{\varepsilon_0}\frac{1}{\mu_0\mu_{xx}},\ m_{Dx3}=\frac{1}{m_{Dx0}}\frac{\Delta t\sigma_x'}{\varepsilon_0}\\
&m_{Hx4}=m_{Dx4}=-\frac{1}{m_{Hx0}}\frac{\Delta t}{{\varepsilon_0}^2}\sigma_y'\sigma_z'
\end{aligned}\tag{3.107}$$

$$\begin{aligned}
&m_{Hy0}=m_{Dy0}=\frac{1}{\Delta t}+\frac{\sigma_x'+\sigma_z'}{2\varepsilon_0}+\frac{\sigma_x'\sigma_z'\Delta t}{4{\varepsilon_0}^2}\\
&m_{Hy1}=m_{Dy1}=\frac{1}{m_{Hy0}}(\frac{1}{\Delta t}-\frac{\sigma_x'+\sigma_z'}{2\varepsilon_0}-\frac{\sigma_x'\sigma_z'\Delta t}{4{\varepsilon_0}^2})\\
&m_{Hy2}=-\frac{1}{m_{Hy0}}\frac{1}{\mu_0\mu_{yy}},m_{Dy2}=\frac{1}{m_{Dy0}}\\
&m_{Hy3}=-\frac{1}{m_{Hy0}}\frac{\Delta t\sigma_y'}{\varepsilon_0}\frac{1}{\mu_0\mu_{yy}},m_{Dy3}=\frac{1}{m_{Dy0}}\frac{\Delta t\sigma_y'}{\varepsilon_0}\\
&m_{Hy4}=m_{Dy4}=-\frac{1}{m_{Hy0}}\frac{\Delta t}{{\varepsilon_0}^2}\sigma_x'\sigma_z'
\end{aligned}\tag{3.108}$$

$$\begin{aligned}
&m_{Hz0}=m_{Dz0}=\frac{1}{\Delta t}+\frac{\sigma_x'+\sigma_y'}{2\varepsilon_0}+\frac{\sigma_x'\sigma_y'\Delta t}{4{\varepsilon_0}^2}\\
&m_{Hz1}=m_{Dz1}=\frac{1}{m_{Hz0}}(\frac{1}{\Delta t}-\frac{\sigma_x'+\sigma_y'}{2\varepsilon_0}-\frac{\sigma_x'\sigma_y'\Delta t}{4{\varepsilon_0}^2})\\
&m_{Hz2}=-\frac{1}{m_{Hz0}}\frac{1}{\mu_0\mu_{zz}},m_{Dz2}=\frac{1}{m_{Dz0}}\\
&m_{Hz3}=-\frac{1}{m_{Hz0}}\frac{\Delta t\sigma_z'}{\varepsilon_0}\frac{1}{\mu_0\mu_{zz}},m_{Dz3}=\frac{1}{m_{Dz0}}\frac{\Delta t\sigma_z'}{\varepsilon_0}\\
&m_{Hz4}=m_{Dz4}=-\frac{1}{m_{Hz0}}\frac{\Delta t}{{\varepsilon_0}^2}\sigma_x'\sigma_y'
\end{aligned}\tag{3.109}$$

doi:10.6342/NTU202501087

$$E_x\Big|_{t+\Delta t}=\frac{1}{\varepsilon_0\varepsilon_{xx}}D_x\Big|_{t+\Delta t} \tag{3.110}$$

$$E_y\Big|_{t+\Delta t}=\frac{1}{\varepsilon_0\varepsilon_{yy}}D_y\Big|_{t+\Delta t} \tag{3.111}$$

$$E_z\Big|_{t+\Delta t}=\frac{1}{\varepsilon_0\varepsilon_{zz}}D_z\Big|_{t+\Delta t} \tag{3.112}$$

Furthermore, for 2-D simulations, the derivatives and conductivity in the z direction are set to zero ($\partial/\partial z=0$ and $\sigma'_z=0$). As a result, Eq. (3.101) ~ (3.106) reduce to

$$H_x\Big|_{t+\Delta t/2}=m_{Hx1}\,H_x\Big|_{t-\Delta t/2}+m_{Hx2}\,C_x^E\Big|_t+m_{Hx3}\,I_{CEx}\Big|_t \tag{3.113}$$

$$H_y\Big|_{t+\Delta t/2}=m_{Hy1}\,H_y\Big|_{t-\Delta t/2}+m_{Hy2}\,C_y^E\Big|_t+m_{Hy3}\,I_{CEy}\Big|_t \tag{3.114}$$

$$H_z\Big|_{t+\Delta t/2}=m_{Hz1}\,H_z\Big|_{t-\Delta t/2}+m_{Hz2}\,C_z^E\Big|_t+m_{Hz4}\,I_{Hz}\Big|_{t-\Delta t/2} \tag{3.115}$$

$$D_x\Big|_{t+\Delta t}=m_{Dx1}\,D_x\Big|_t+m_{Dx2}\,C_x^H\Big|_{t+\Delta t/2}+m_{Dx3}\,I_{CHx}\Big|_{t+\Delta t/2} \tag{3.116}$$

$$D_y\Big|_{t+\Delta t}=m_{Dy1}\,D_y\Big|_t+m_{Dy2}\,C_y^H\Big|_{t+\Delta t/2}+m_{Dy3}\,I_{CHy}\Big|_{t+\Delta t/2} \tag{3.117}$$

$$D_z\Big|_{t+\Delta t}=m_{Dz1}\,D_z\Big|_t+m_{Dz2}\,C_z^H\Big|_{t+\Delta t/2}+m_{Dz4}\,I_{Dz}\Big|_t \tag{3.118}$$

Also, the discrete curl operator coefficients in Eq. (3.99) reduce to

$$\begin{aligned}
C_x^E\Big|_t &= IFFT_y\{ik_y\times FFT_y\{E_z\Big|_t\}\}\\
C_y^E\Big|_t &= -IFFT_x\{ik_x\times FFT_x\{E_z\Big|_t\}\}\\
C_z^E\Big|_t &= IFFT_x\{ik_x\times FFT_x\{E_y\Big|_t\}\}-IFFT_y\{ik_y\times FFT_y\{E_x\Big|_t\}\}\\
C_x^H\Big|_t &= IFFT_y\{ik_y\times FFT_y\{H_z\Big|_{t+\Delta t/2}\}\}\\
C_y^H\Big|_t &= -IFFT_x\{ik_x\times FFT_x\{H_z\Big|_{t+\Delta t/2}\}\}\\
C_z^H\Big|_t &= IFFT_x\{ik_x\times FFT_x\{H_y\Big|_{t+\Delta t/2}\}\}-IFFT_y\{ik_y\times FFT_y\{H_x\Big|_{t+\Delta t/2}\}\}
\end{aligned} \tag{3.119}$$

and the coefficients in Eq. (3.107) ~ (3.109) reduce to

$$\begin{aligned}
m_{Hx0} &= m_{Dx0} = \frac{1}{\Delta t} + \frac{\sigma'_y}{2\varepsilon_0} \\
m_{Hx1} &= m_{Dx1} = \frac{1}{m_{Hx0}}\left(\frac{1}{\Delta t} - \frac{\sigma'_y}{2\varepsilon_0}\right) \\
m_{Hx2} &= -\frac{1}{m_{Hx0}}\frac{1}{\mu_0\mu_{xx}}, m_{Dx2} = \frac{1}{m_{Dx0}} \\
m_{Hx3} &= -\frac{1}{m_{Hx0}}\frac{\Delta t\sigma'_x}{\varepsilon_0}\frac{1}{\mu_0\mu_{xx}}, m_{Dx3} = \frac{1}{m_{Dx0}}\frac{\Delta t\sigma'_x}{\varepsilon_0}
\end{aligned} \tag{3.120}$$

$$\begin{aligned}
m_{Hy0} &= m_{Dy0} = \frac{1}{\Delta t} + \frac{\sigma'_x}{2\varepsilon_0} \\
m_{Hy1} &= m_{Dy1} = \frac{1}{m_{Hy0}}\left(\frac{1}{\Delta t} - \frac{\sigma'_x}{2\varepsilon_0}\right) \\
m_{Hy2} &= -\frac{1}{m_{Hy0}}\frac{1}{\mu_0\mu_{yy}}, m_{Dy2} = \frac{1}{m_{Dy0}} \\
m_{Hy3} &= -\frac{1}{m_{Hy0}}\frac{\Delta t\sigma'_y}{\varepsilon_0}\frac{1}{\mu_0\mu_{yy}}, m_{Dy3} = \frac{1}{m_{Dy0}}\frac{\Delta t\sigma'_y}{\varepsilon_0}
\end{aligned} \tag{3.121}$$

$$\begin{aligned}
m_{Hz0} &= m_{Dz0} = \frac{1}{\Delta t} + \frac{\sigma'_x + \sigma'_y}{2\varepsilon_0} + \frac{\sigma'_x\sigma'_y\Delta t}{4{\varepsilon_0}^2} \\
m_{Hz1} &= m_{Dz1} = \frac{1}{m_{Hz0}}\left(\frac{1}{\Delta t} - \frac{\sigma'_x + \sigma'_y}{2\varepsilon_0} - \frac{\sigma'_x\sigma'_y\Delta t}{4{\varepsilon_0}^2}\right) \\
m_{Hz2} &= -\frac{1}{m_{Hz0}}\frac{1}{\mu_0\mu_{zz}}, m_{Dz2} = \frac{1}{m_{Dz0}} \\
m_{Hz4} &= m_{Dz4} = -\frac{1}{m_{Hz0}}\frac{\Delta t}{{\varepsilon_0}^2}\sigma'_x\sigma'_y
\end{aligned} \tag{3.122}$$

Eq. (3.113), (3.114), and (3.118) only have the terms H_x, H_y, E_z and D_z are called TM mode. Similarly, Eq. (3.115), (3.116), and (3.117) only have the terms E_x, D_x, E_y, D_y, and H_z are called TE mode. The six equations, along with the three electric field constitutive relations, construct the fundamental PSTD algorithm with the PML in 2-D simulation space.

Chapter 4 Results and Discussion

In this chapter, we first outline the simulation model in Section 4.1. Next, we organize the simulation results in Section 4.2. Finally, Section 4.3 provides a series of subsequent discussions about the EAOPC and CAOPC techniques.

4.1 Simulation Model

This section introduces the simulation environment and the simulation scheme for the EAOPC and CAOPC techniques. In Section 4.1.1, we detail the simulation settings. In Section 4.1.2, we describe the simulation approach for EAOPC and CAOPC in which the OPC process is divided into forward and backward scenarios.

4.1.1 Simulation Settings

In this research, all simulations are conducted in 2-D, modeling the propagation of TM waves in scattering media. A schematic of the simulation setup is shown in Fig. 4.1. Each side of a 600 μm × 600 μm simulation region is discretized into 1800 cells, resulting in a cell size of $1/3$ μm. A time step $\Delta t = 0.05$ fs is chosen to meet the Courant stability condition. Every simulation has 120000 time steps; the corresponding simulation time is 6 ps. A CW light source, compacted in a 2.5 μm by 40 μm space, is centered in the simulation environment. The waves propagate in the positive x direction with a Gaussian modulated amplitude in the y direction and a wavelength of 1 μm. N dielectric cylinders (ranging from 0 to 1600), each with a radius of 3 μm and a refractive index of 1.2, are randomly positioned in an annulus, having inner and outer radii of 25 μm and 180 μm, respectively. A ring OPC region has a radius ranging from 290 μm to

doi:10.6342/NTU202501087

295 µm, with its center at the simulation space's center. A PML absorbing boundary condition is employed to eliminate reflections of outgoing waves. Finally, an interface is placed 5 µm from the light source for quantitative analyses.

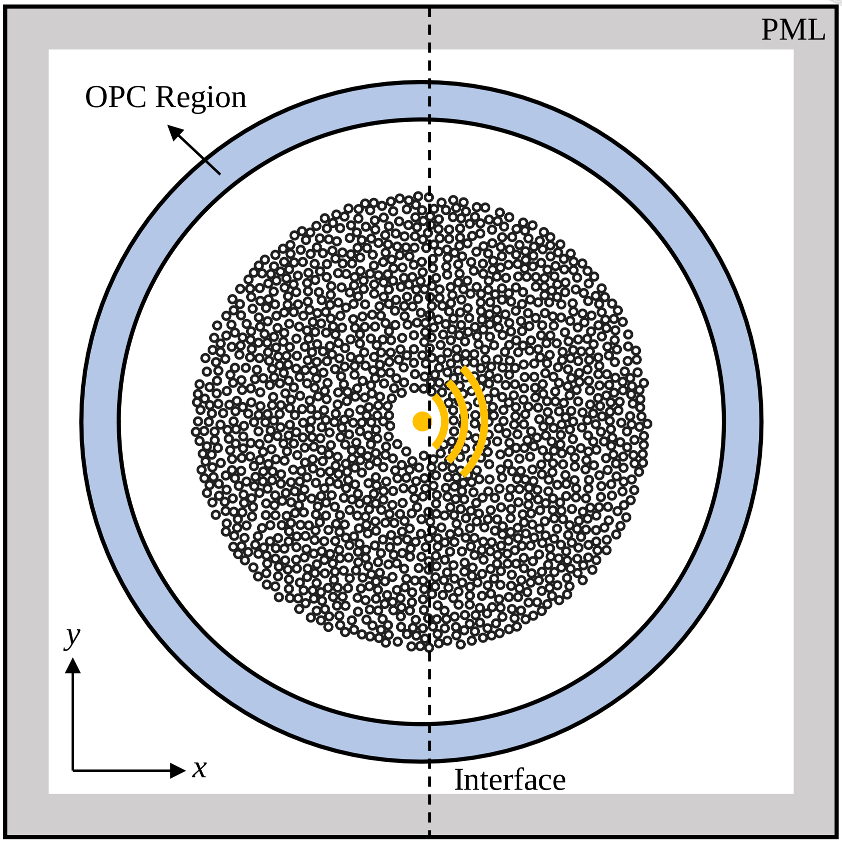

Fig. 4.1 A schematic of the PSTD simulation setup for OPC light refocusing in a scattering medium with 1600 scatterers.

4.1.2 Forward and Backward Scenarios

The scheme we use to implement the OPC phenomenon is dividing the simulation into forward and backward scenarios. The forward scenario illustrates light scattering in a turbid medium, while the backward scenario demonstrates light refocusing via EAOPC and CAOPC. In this section, we provide a comprehensive interpretation of the scheme by visualizing both scenarios, with the simulation case of 1600 scatterers ($N = 1600$) serving as a representative example.

doi:10.6342/NTU202501087

The forward scenario is shown in Fig. 4.2. A CW source is placed at the center of a scattering medium. When the waves pass through the scattering medium, they travel through intricate optical paths due to light scattering. According to the Huygens principle, the scattering effect creates multiple virtual tiny light sources, and the emitted waves interfere to build a speckle pattern in an OPC region. Meanwhile, the OPC region acts as a detector and captures the amplitude and phase information of the speckle pattern by calculating the phasor at a frequency of 300 THz. Hence, each segment in the OPC region has its own amplitude and phase (schematically represented as E_1 to E_4 and φ_1 to φ_4), revealing constructive and destructive interference zones and areas in between.

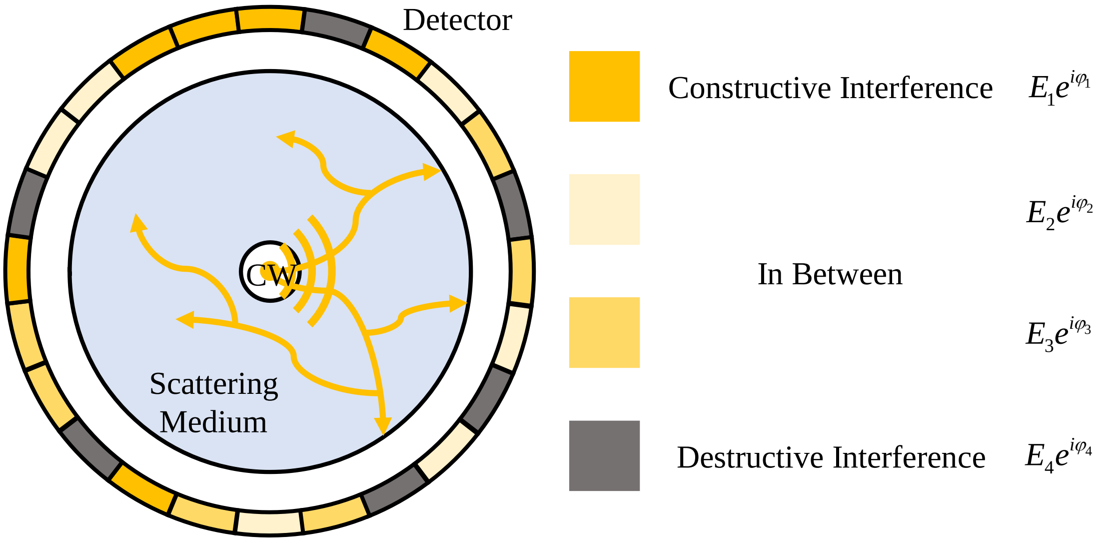

Fig. 4.2 A schematic of the forward scenario. Scattered waves interfere to build a speckle pattern, which is recorded in the OPC region.

Here, we depict normalized electric field intensity distributions in Fig. 4.3 to demonstrate light scattering in the forward scenario. In comparison to light propagation in a vacuum (Fig. 4.3 (a)), the waves are multiply scattered by 1600 scatterers randomly distributed inside the annulus, interfering to create complicated optical paths in the scattering medium (Fig. 4.3 (b)).

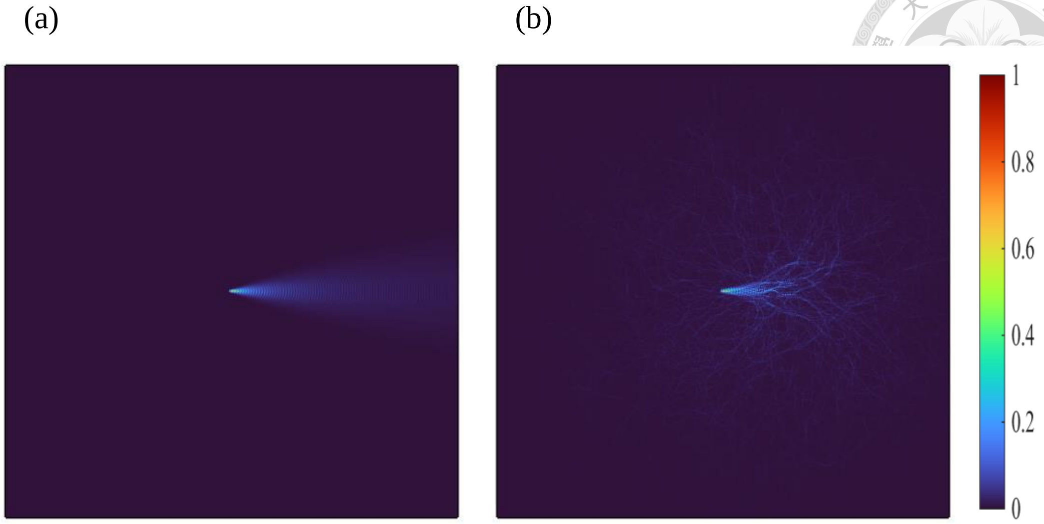

Fig. 4.3 Normalized electric field intensity distributions in (a) a vacuum and (b) a medium with 1600 scatterers at 3 ps in the forward scenario. Comparing (b) with (a), random light scattering creates intricate optical paths, resulting in a complex electric field intensity distribution.

Also, the recorded amplitude and phase information are shown in Fig. 4.4 (a) and Fig. 4.4 (b), respectively. Each pixel in the OPC region has a specific amplitude and phase.

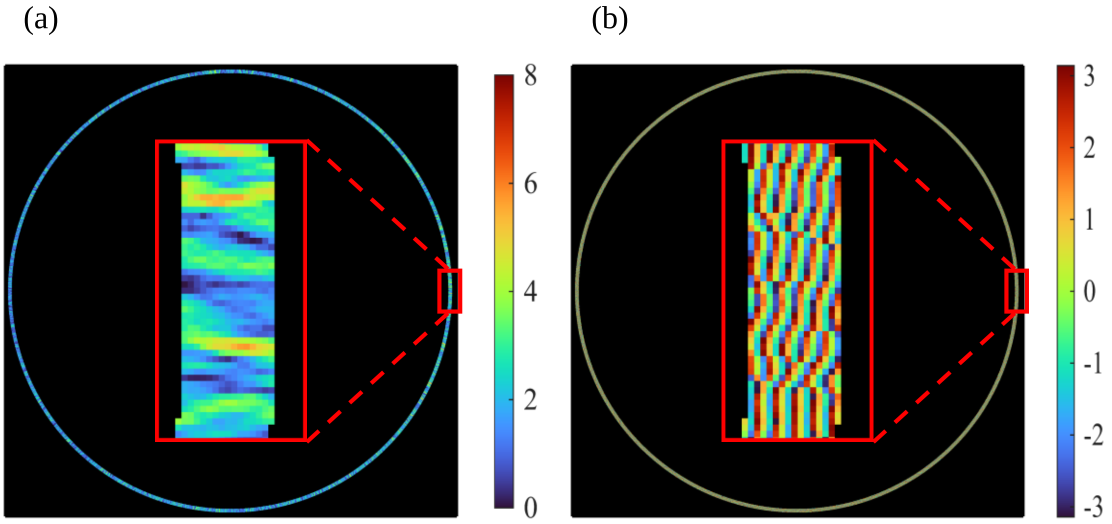

Fig. 4.4 Recorded (a) amplitude and (b) phase distributions within the OPC region in the forward scenario. The inset shows a magnified view of a rectangular area along the right edge of the OPC region, with a width of 8 μm and a height of 16 μm. The amplitude is measured in volts per meter (V/m), and the phase is given in radians, wrapped to the range of -π to π (mod 2π).

Next, the EA backward scenario is shown in Fig. 4.5. In this scenario, each segment in the OPC region acts as a tiny source with the identical amplitude that we record in the forward scenario (E_1 to E_4) and a conjugated phase ($-\varphi_1$ to $-\varphi_4$). Then, as emitted waves from all sources propagate back through the scattering medium, they retrace their previous scattering optical paths. The phases are canceled by traveling through the same scattering medium, and the waves constructively interfere at the original source region to build a focus. Finally, when the simulation reaches a steady state, the light is successfully refocused at the original source region.

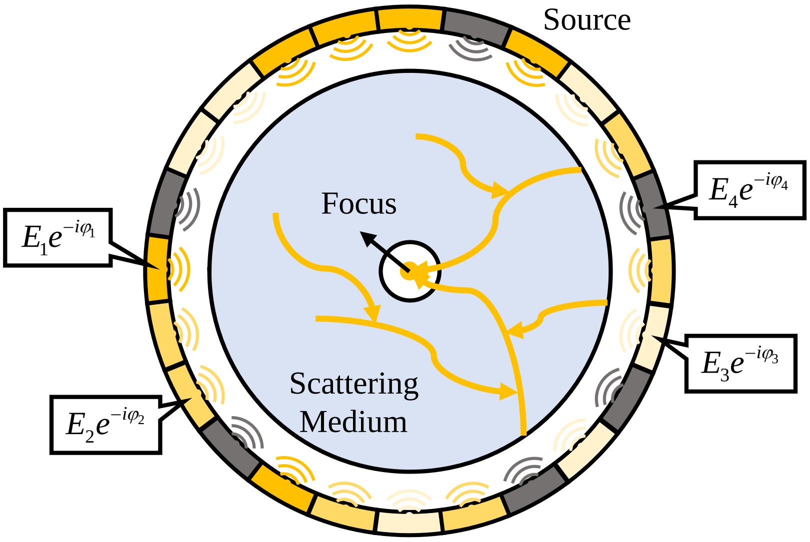

Fig. 4.5 A schematic of the EA backward scenario. Each segment in the OPC region becomes a source with the EA and a conjugated phase. By canceling the phases, the emitted waves form constructive interference at the original source region. Finally, the waves are refocused when the simulation reaches a steady state.

In the EA backward simulation, the amplitude distribution of the pixels in the OPC region is shown in Fig. 4.4 (a), which is identical to the amplitude distribution recorded in the forward scenario. In contrast, the phase distribution is conjugated to the recorded phase distribution (Fig. 4.4 (b)), as illustrated in Fig. 4.6.

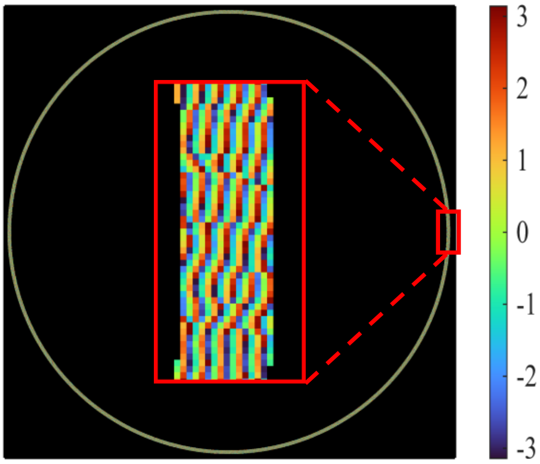

Fig. 4.6 Phase distribution within the OPC region in the EA backward scenario. The distribution is conjugated to the recorded phase distribution in the forward scenario. The inset shows a magnified view of a rectangular area along the right edge of the OPC region, with a width of 8 μm and a height of 16 μm. The phase is given in radians, wrapped to the range of -π to π (mod 2π).

Then, we plot normalized electric field intensity distributions in Fig. 4.7 to show light refocusing in the EA backward scenario. Traveling through the same optical paths as in the forward scenario (Fig. 4.7 (a)), the waves refocus at the source region in the steady state (Fig. 4.7 (b)).

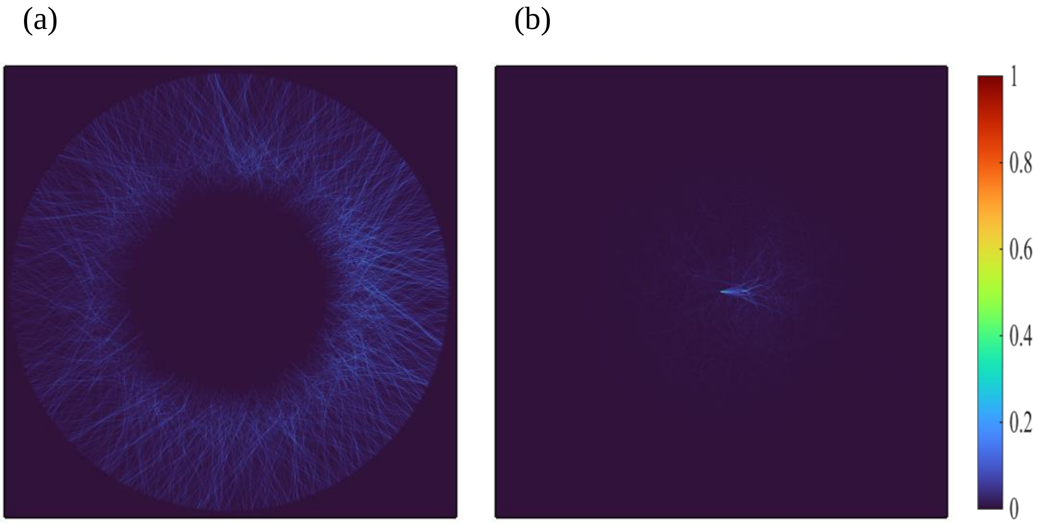

Fig. 4.7 Normalized electric field intensity distributions at (a) 0.6 ps and (b) 6 ps in the EA backward scenario. (a) and (b) show snapshots of light propagation in the EA backward scenario.

Finally, the CA backward scenario is shown in Fig. 4.8. Here, we aim to perform OPC's backward light refocusing process without the recorded amplitude information. To accomplish this, we deliberately eliminate the amplitude variations by applying a CA E_0 across all segments in the OPC region to remove any dependence on the recorded amplitude distribution. On the other hand, the phase of each segment remains unchanged ($-\varphi_1$ to $-\varphi_4$).

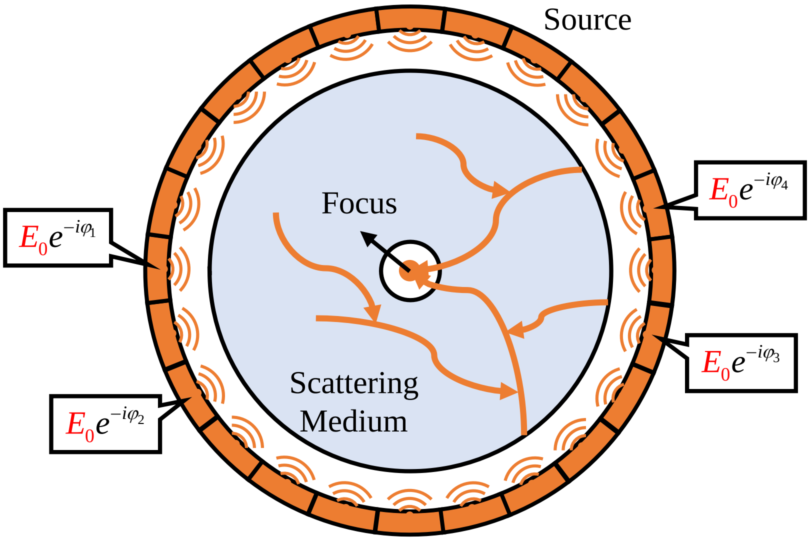

Fig. 4.8 A schematic of the CA backward scenario. Compared to the EA backward scenario, each segment in the OPC region is a source having the same amplitude. However, the phase of each segment is kept. We execute the same simulation as in the EA backward scenario with this scheme to investigate the differences between EAOPC and CAOPC.

In the CA backward simulation, the amplitudes of all pixels in the OPC region are set to the root-mean-square (RMS) value of the recorded data in the forward scenario, as shown in Fig. 4.9. The RMS value calculated by Eq. (4.1) ensures that energy conservation is maintained for both the EA and CA cases.

$$E_{CA} = \sqrt{\frac{1}{N}\sum_{n=1}^{N}(E_n)^2} \tag{4.1}$$

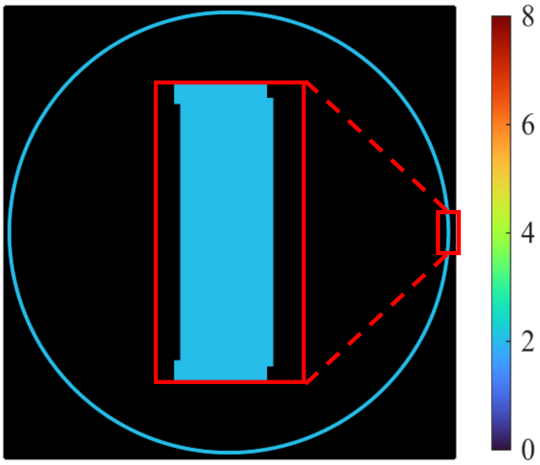

Fig. 4.9 Amplitude distribution within the OPC region in the CA backward scenario. The amplitudes of all pixels are set to 2.035 V/m, the RMS value of the recorded data in the forward scenario. The inset shows a magnified view of a rectangular area along the right edge of the OPC region, with a width of 8 μm and a height of 16 μm.

Also, the phases of all pixels in the OPC region are the same as those in the EA backward scenario (Fig. 4.6). Normalized electric field intensity distributions in Fig. 4.10 show the following light refocusing in the CA backward scenario. The differences between the CA and EA backward scenarios are presented in Section 4.2.

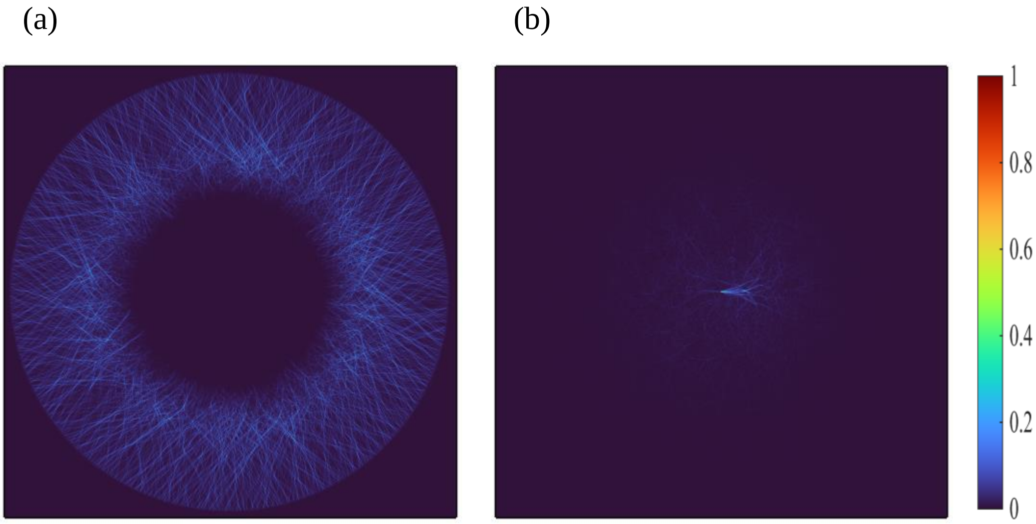

Fig. 4.10 Normalized electric field intensity distributions at (a) 0.6 ps and (b) 6 ps in the CA backward scenario. (a) and (b) show snapshots of light propagation in the CA backward scenario.

doi:10.6342/NTU202501087

4.2 Simulation Results

We perform simulations of EAOPC and CAOPC across various scatterer number densities (ranging from 100 to 1600). Before presenting the outcomes, we first introduce the analysis methods and evaluation metrics used throughout this study. The results will then be examined in detail based on these approaches.

The time-reversal property of OPC indicates that the waves should refocus at the source region and reconstruct the initial electric field profile of the source. In the simulations, the initial and refocused electric field profiles at the interface are computed in the forward and backward scenarios, respectively, by calculating the amplitude of the phasor at a frequency of 300 THz. Therefore, the electric field distributions at the interface in the forward and backward scenarios must be the same. In other words, the consistency between the forward and backward electric field distributions at the interface can be a measure of OPC light refocusing effectiveness.

To quantitatively analyze the consistency between the two electric field distributions in the forward and backward scenarios, we employ the RMS error defined in Eq. (4.2).

$$Error = \sqrt{\frac{\sum_{i=1}^{N}[E_{\mathrm{backward}}(i) - E_{\mathrm{forward}}(i)]^2}{N}} \tag{4.2}$$

Here, N is the total number of cells at the interface. For each simulation, we depict the steady-state electric field distributions at the interface for both forward and backward scenarios and compute the RMS error between them. For EAOPC, the error directly reflects its effectiveness. For CAOPC, however, since the ideal case varies with the scattering condition, we evaluate its performance by comparing the error with that of EAOPC under the same scatterer number density. In the following, we present the simulation results and key findings.

doi:10.6342/NTU202501087

We first examine the effectiveness of both OPC techniques in sparse media. Here, we use the scattering media with 100 and 200 scatterers as illustrative examples. The corresponding distributions of the forward and backward electric fields for each case are presented in Fig. 4.11. For the EAOPC technique, the forward and backward electric field distributions have an RMS error of 0.188 V/m in the medium with 100 scatterers and an RMS error of 0.237 V/m in the medium with 200 scatterers. On the other hand, the CAOPC technique yields RMS errors of 2.606 V/m and 2.143 V/m in the media with 100 and 200 scatterers, respectively.

These results demonstrate that the EAOPC technique achieves a much more effective light refocusing process than the CAOPC technique in sparse scattering environments. The relatively minor errors observed with the EAOPC technique indicate that the forward and backward electric field distributions are closely matched, signifying a precise reconstruction of the original electric field profile of the source and a successful light refocusing. On the other hand, the larger errors associated with the CAOPC technique reveal that the forward and backward electric field distributions are poorly matched, highlighting a worse reconstruction and light refocusing process than the EAOPC technique.

Additionally, the significant differences in the RMS errors observed between the EAOPC and CAOPC techniques lead to a clear and substantial disparity in their overall light refocusing performance in sparse scattering conditions. This stark contrast in performance between the two techniques provides a critical insight: while the EAOPC technique is able to achieve effective light refocusing in sparse media, the CAOPC technique struggles to deliver comparable results. The evident performance gap suggests that the CAOPC technique is unsuitable for light refocusing in sparsely scattering environments.

doi:10.6342/NTU202501087

(a) N = 100, EAOPC

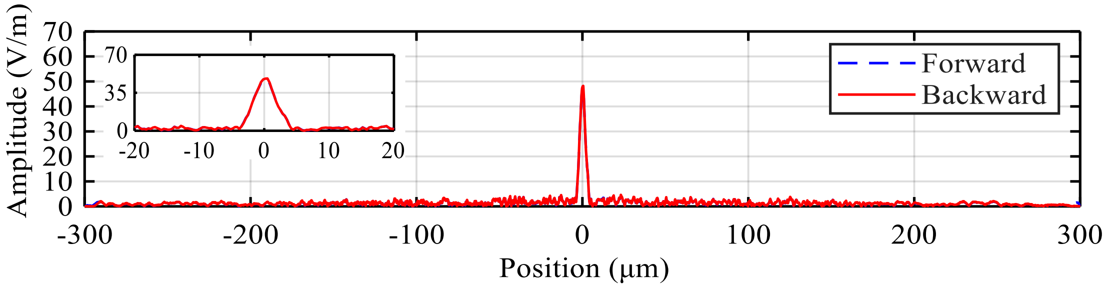

(b) N = 100, CAOPC

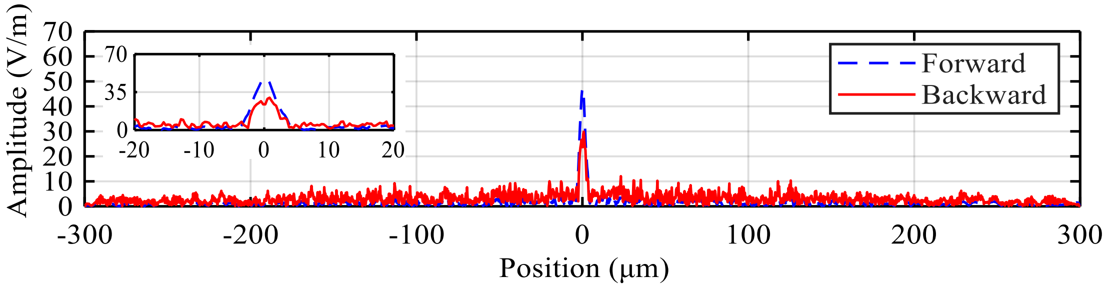

(c) N = 200, EAOPC

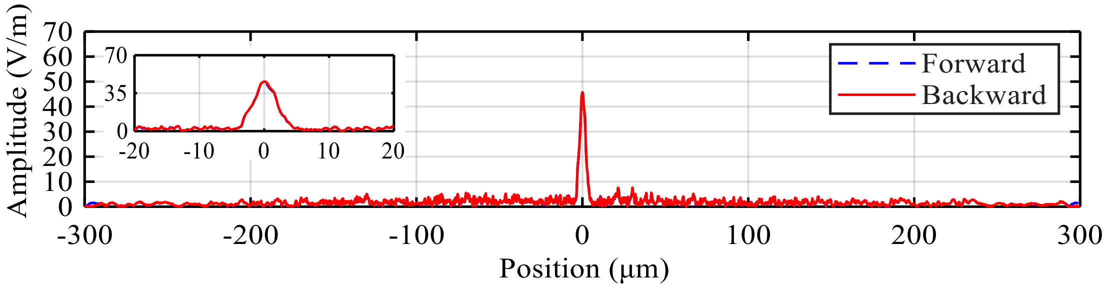

(d) N = 200, CAOPC

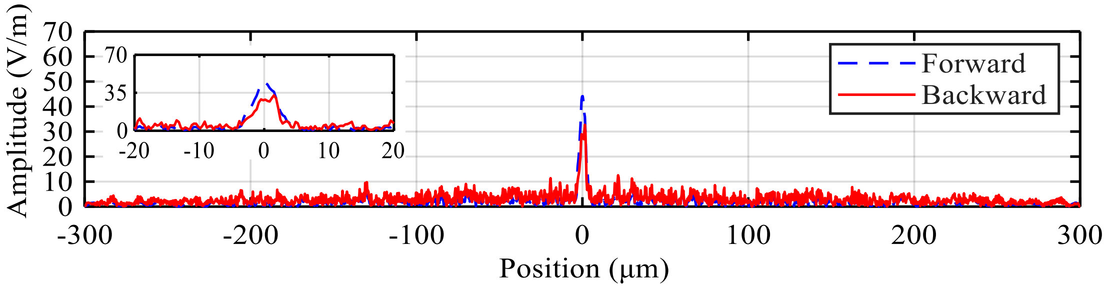

Fig. 4.11 Steady-state electric field distributions at the interface for forward and backward scenarios under different conditions: (a) with 100 scatterers via EAOPC, (b) with 100 scatterers via CAOPC, (c) with 200 scatterers via EAOPC, and (d) with 200 scatterers via CAOPC. The inset shows a magnified view between -20 μm and 20 μm. Comparing (a) and (c) with (b) and (d), EAOPC demonstrates significantly superior light refocusing performance in comparison to CAOPC, implying that the CAOPC technique is not applicable in sparse media.

Then, we increase the scatterer number density to further examine the effectiveness of both OPC techniques in denser media. Specifically, we consider the cases of 800 and 900 scatterers as representative conditions of denser media. The corresponding electric field distributions for both forward and backward scenarios are illustrated in Fig. 4.12. For the EAOPC technique, the RMS errors between the forward and backward electric field distributions are calculated to be 0.659 V/m in the medium with 800 scatterers and 0.769 V/m in the medium with 900 scatterers. On the other hand, for the CAOPC technique, the RMS errors between the forward and backward electric field distributions are found to be 1.188 V/m in the medium with 800 scatterers and 1.270 V/m in the medium with 900 scatterers.

These results reveal several important trends. First, these slightly increased RMS error values in the EAOPC technique, compared to the sparse media cases, indicate that the performance of light refocusing via EAOPC experiences a modest decline as the scatterer number density increases. Additionally, the RMS errors of the CAOPC technique remain larger than those in the EAOPC technique, revealing that increasing scatterer number density does not make CAOPC superior to EAOPC.

However, in these denser scattering conditions, the differences in the RMS errors between the EAOPC and CAOPC techniques become smaller, indicating that the performance gap between the two techniques narrows as the scatterer number density increases. In other words, this convergence of performance suggests that the CAOPC technique, while initially less effective in sparse media, becomes progressively more enhanced and begins to approach the light refocusing capability of the EAOPC technique in denser media. The noticeable reduction in the performance gap demonstrates that the applicability of the CAOPC technique significantly improves in denser scattering environments.

(a) N = 800, EAOPC

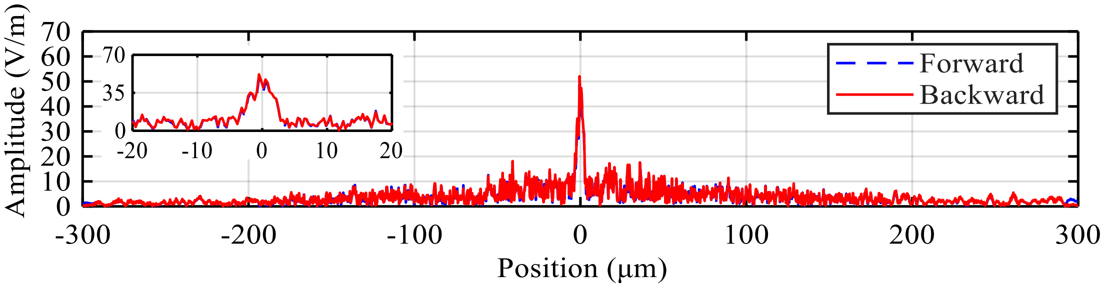

(b) N = 800, CAOPC

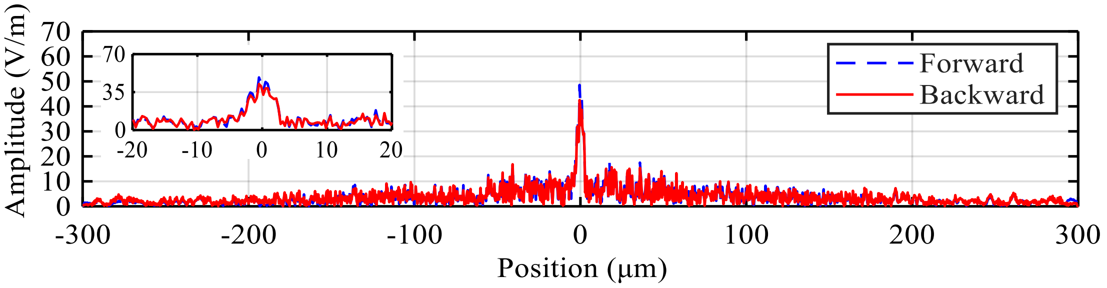

(c) N = 900, EAOPC

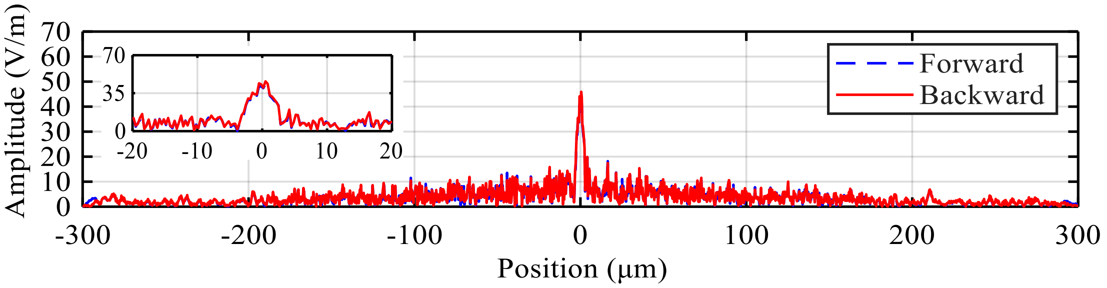

(d) N = 900, CAOPC

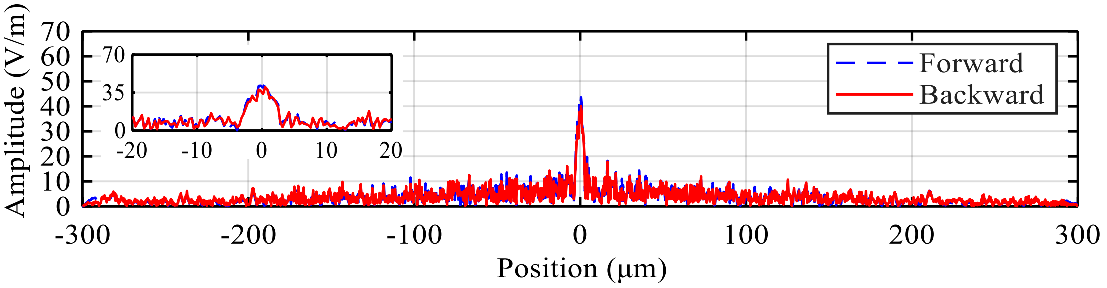

Fig. 4.12 Steady-state electric field distributions at the interface for forward and backward scenarios under different conditions: (a) with 800 scatterers via EAOPC, (b) with 800 scatterers via CAOPC, (c) with 900 scatterers via EAOPC, and (d) with 900 scatterers via CAOPC. The inset shows a magnified view between -20 μm and 20 μm. Comparing Fig. 4.12 with Fig. 4.11, CAOPC demonstrates a better light refocusing performance in denser media, implying that the CAOPC technique gradually becomes more applicable as the scatterer number density increases.

Next, we examine the effectiveness of both OPC techniques in dense media. In particular, media containing 1500 and 1600 scatterers are investigated as representative instances of dense scattering environments. The corresponding electric field distributions for both forward and backward scenarios are depicted in Fig. 4.13. For the EAOPC technique, the RMS errors between the forward and backward electric field distributions are measured to be 1.714 V/m and 2.110 V/m for media containing 1500 and 1600 scatterers, respectively. On the other hand, for the CAOPC technique, the RMS errors between the forward and backward electric field distributions are 2.115 V/m and 2.526 V/m under the same scattering conditions.

These results reproduce the phenomena we observed in the media with 800 and 900 scatterers. First, the RMS errors of the EAOPC technique keep increasing as the scatterer number density increases, indicating that the performance of light refocusing using EAOPC continues to reduce as the scattering condition becomes more complex. In addition, the CAOPC technique still produces greater RMS errors than the EAOPC technique, confirming that the EAOPC technique is a better scheme than the CAOPC technique for light refocusing in scattering media.

Furthermore, the differences in the RMS errors between the EAOPC and CAOPC techniques remain decreasing as the scatterer number density increases. The gradually converging performance gap indicates that the CAOPC technique behaves similarly to the EAOPC technique in dense media. That is, in comparison to the CAOPC technique in sparse media, it can produce results comparable to those of the EAOPC technique and approach the light refocusing ability of the EAOPC technique in dense media. Consequently, the narrowing performance gap between the two techniques demonstrates that the CAOPC technique can achieve effective light refocusing and becomes applicable in dense scattering environments.

doi:10.6342/NTU202501087

(a) N = 1500, EAOPC

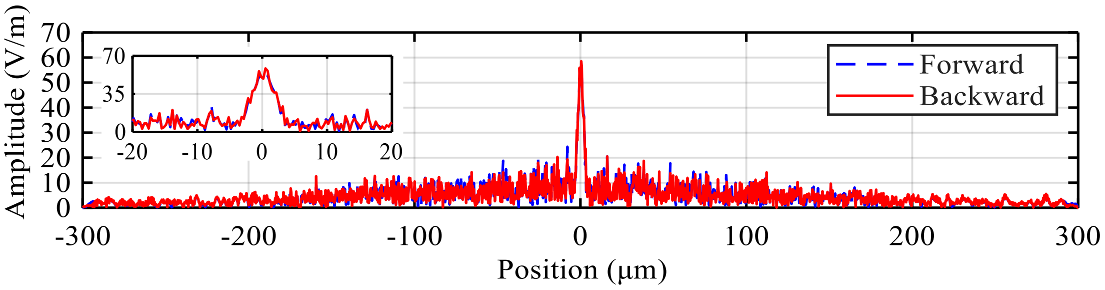

(b) N = 1500, CAOPC

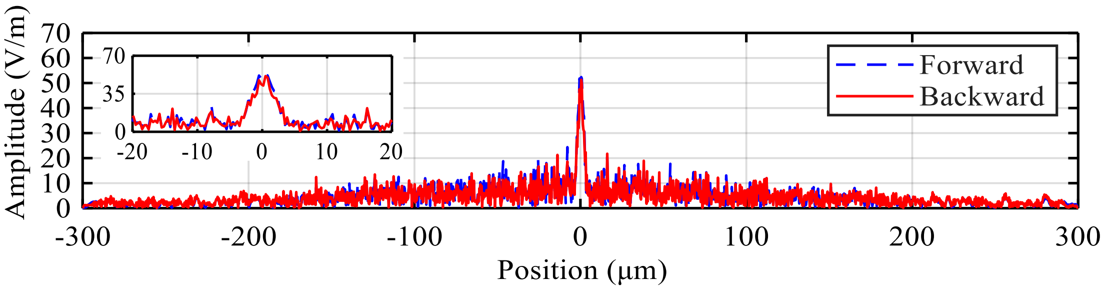

(c) N = 1600, EAOPC

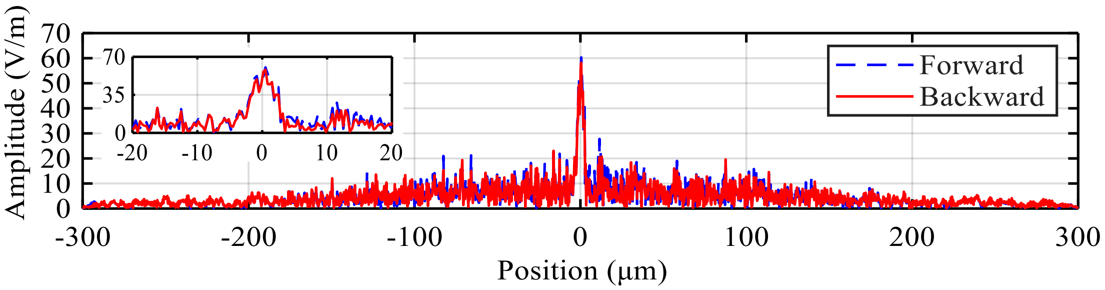

(d) N = 1600, CAOPC

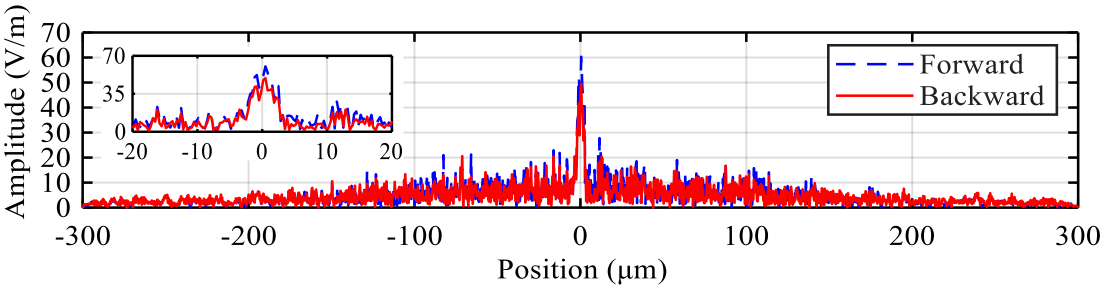

Fig. 4.13 Steady-state electric field distributions at the interface for forward and backward scenarios under different conditions: (a) with 1500 scatterers via EAOPC, (b) with 1500 scatterers via CAOPC, (c) with 1600 scatterers via EAOPC, and (d) with 1600 scatterers via CAOPC. The inset shows a magnified view between -20 μm and 20 μm. Comparing (a) and (c) with (b) and (d), CAOPC demonstrates a comparable light refocusing performance to EAOPC, implying that the CAOPC technique is applicable in dense media.

Finally, we organize the results of EAOPC and CAOPC across different scattering media, with the number of scatterers ranging from 100 to 1600, into a line chart for a more straightforward comparison. As depicted in Fig. 4.14, we plot a line chart showing the variation of RMS error with varying scatterer number density for both EAOPC and CAOPC. Meanwhile, the numerical data corresponding to the plotted lines are detailed in Table 4.1 for reference.

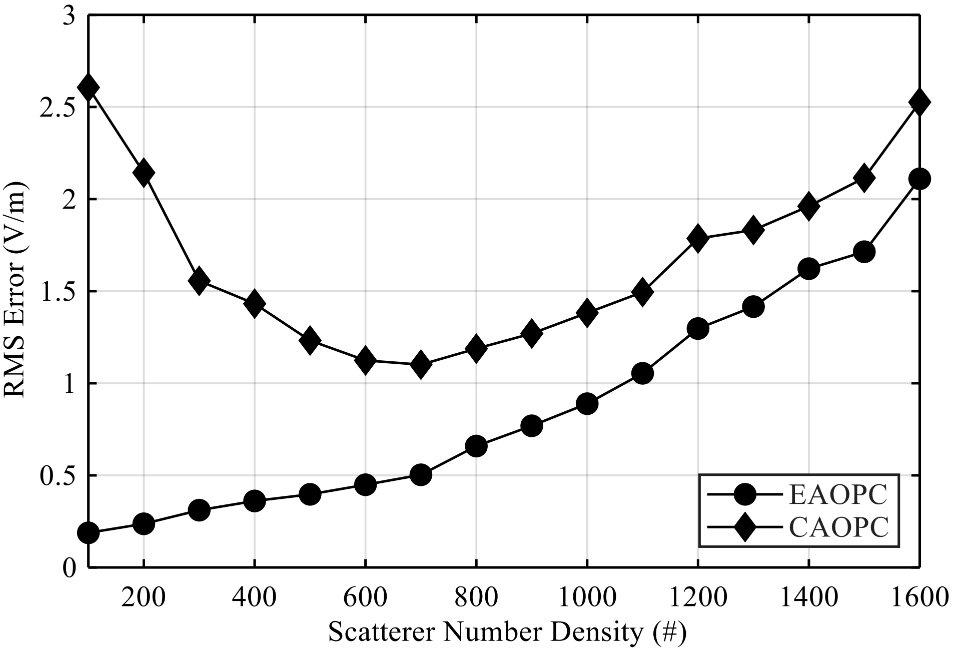

Fig. 4.14 A line chart showing the RMS error variation with various scatterer number densities via EAOPC and CAOPC. The chart reveals three key findings: 1. EAOPC performs better than CAOPC under the same scatterer number density. 2. The performance of EAOPC decreases as the scatterer number density increases. 3. CAOPC works in dense media but not in sparse media.

Through Fig. 4.14, we highlight three key findings about the EAOPC and CAOPC techniques in different scattering conditions.

1. EAOPC outperforms CAOPC under the same scatterer number density.
2. The performance of EAOPC declines with increasing scatterer number density.
3. CAOPC is applicable in dense media but not in sparse media.

Table. 4.1 RMS errors of EAOPC and CAOPC in scattering media containing 100 to 1600 scatterers. The data listed in this table correspond to the data points plotted in Fig. 4.14.

Scatterer Number Density (#)	**RMS Error (V/m)**	
	via EAOPC	**via CAOPC**
100	0.188	2.606
200	0.237	2.143
300	0.311	1.556
400	0.361	1.432
500	0.397	1.232
600	0.449	1.124
700	0.503	1.101
800	0.659	1.188
900	0.769	1.270
1000	0.889	1.382
1100	1.054	1.495
1200	1.297	1.786
1300	1.416	1.832
1400	1.622	1.961
1500	1.714	2.115
1600	2.110	2.526

doi:10.6342/NTU202501087

4.3 Discussion on the Findings of Optical Phase Conjugation With and Without Amplitude Information

In this section, we first discuss the three findings in Section 4.2. We then provide explanations for these phenomena. Finally, we conclude the differences between EAOPC and CAOPC, namely, OPC light refocusing with and without amplitude information.

1. EAOPC outperforms CAOPC under the same scatterer number density.

Under the same scatterer number density, EAOPC has a smaller RMS error than CAOPC. This suggests that it is more effective in achieving precise light refocusing. Therefore, EAOPC has better performance than CAOPC.

The explanation for the better performance of EAOPC is as follows: Light travels through a scattering medium, creating a speckle pattern that carries both amplitude and phase information. Since the speckle pattern forms through interference, the stronger constructive interference regions have higher amplitudes. When we apply the CAOPC technique, we calculate the RMS value of the amplitudes on the speckle pattern. This approach lowers the amplitudes in these high-amplitude areas and redistributes them to regions with lower amplitudes. However, these lower-amplitude regions represent areas with destructive interference, so energy can’t be delivered efficiently, leading to reduced light refocusing performance. Put differently, the amplitude information contributes to an optimized amplitude distribution strategy for OPC light refocusing as the strategy distributes the larger amplitude to the higher constructive interference regions, where energy transfer is effective, and the smaller amplitude to the lower constructive interference regions, where energy transfer is less effective. Therefore, EAOPC employs a superior amplitude distribution scheme and outperforms CAOPC.

doi:10.6342/NTU202501087

2. The performance of EAOPC declines with increasing scatterer number density. The EAOPC error line in Fig. 4.14 exhibits a monotonic increase with increasing scatterer number density. This suggests reduced EAOPC effectiveness in denser media. In other words, the performance of EAOPC deteriorates in more strongly scattering environments.

The mechanism behind the behavior can be explained by the following: As the scatterer number density increases, waves experience a more complex and chaotic scattering process. The enhanced complexity of wave interactions with the dense medium messes up the phase information, reducing the regions where constructive interference occurs. This makes light refocusing using EAOPC more challenging. Therefore, the effectiveness of the EAOPC technique declines as the scatterer number density increases.

3. CAOPC is applicable in dense media but not in sparse media. The CAOPC technique produces an entirely different result compared to the EAOPC technique. The differences in the RMS errors between the two techniques initially are significant in sparse media. However, as the scatterer number density increases, the differences in the errors become smaller. This means CAOPC performs much worse than EAOPC in sparse media but approaches EAOPC in dense media. Hence, CAOPC can be applied in dense media but not in sparse media.

The reason behind this phenomenon is the uniformity of scattered waves. In dense media, waves undergo multiple scattering events, and the scattered waves propagate in all directions to every pixel in the OPC region. Therefore, the recorded amplitude information in the OPC region is nearly uniform and can be considered a constant. As a result, the CAOPC technique achieves the EAOPC technique, leading to smaller RMS errors and effective light refocusing in dense media. On the other hand, in sparse media, the waves are not scattered uniformly. Therefore, the exact amplitude on each pixel in the

doi:10.6342/NTU202501087

OPC region cannot be represented by a constant. As a result, the CAOPC technique deviates from the EAOPC technique, leading to larger RMS errors and ineffective light refocusing in sparse media.

We can examine the similarity by directly comparing the electric field distributions of the CAOPC and EAOPC techniques. As shown in Fig. 4.15, when the scatterer number density increases from 100 to 1600, the electric field distributions of CAOPC progressively become closer to those of EAOPC. Hence, in dense media, waves scatter uniformly, enabling CAOPC to achieve EAOPC and making CAOPC applicable for light refocusing, whereas in sparse media, this uniformity is absent.

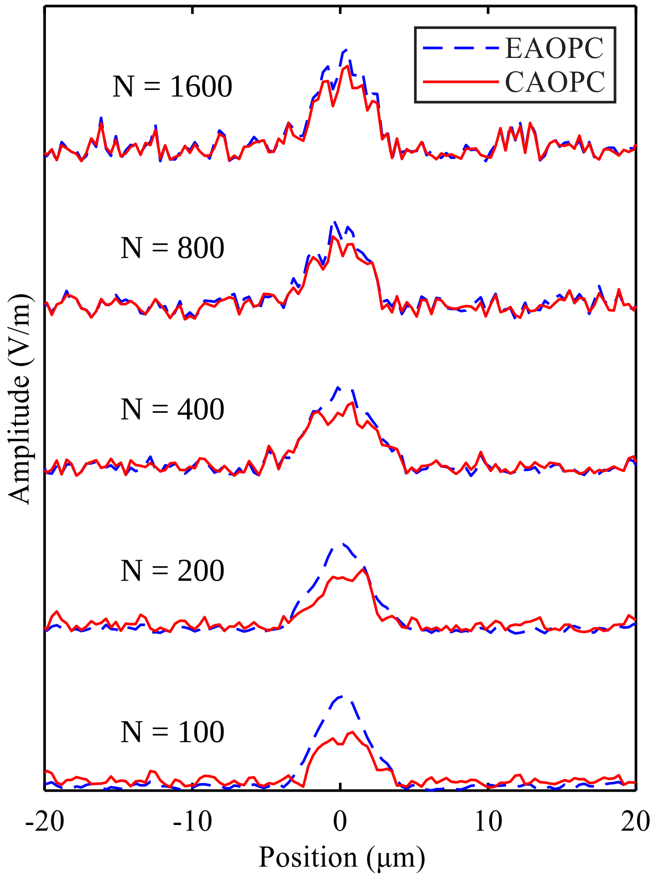

Fig. 4.15 Steady-state electric field distributions at the interface between -20 μm and 20 μm via EAOPC and CAOPC in the media where the number of scatterers doubles sequentially from 100 to 1600. The CAOPC distributions gradually approach those of EAOPC as the scatterer number density increases, implying that the CAOPC technique applies in dense media but not in sparse media.

In conclusion, with the engagement of amplitude information, the EAOPC technique adopts a more effective amplitude distribution strategy and achieves superior performance compared to the CAOPC technique. However, its performance is reduced by increasing the scatterer number density. Also, light refocusing via OPC primarily demands fine phase modulation at each part of the OPC region, involving the adjustment of a huge number of parameters. Under such conditions, simultaneously modulating the amplitudes across the OPC region dramatically increases the optimization burden, which complicates the process and reduces the overall efficiency. Therefore, in dense media, where scattered waves exhibit a high degree of uniformity, CAOPC behaves similarly and demonstrates performance comparable to EAOPC, making it a viable alternative when implementation simplicity or computational cost is a concern.

doi:10.6342/NTU202501087

Chapter 5 Summary and Future Work

This chapter is divided into two sections. In Section 5.1, we summarize this research, from the motivation to the results. Finally, in Section 5.2, we outline potential avenues for future research to investigate this topic further.

5.1 Summary

The motivation of this research originates from the observation of DOPC. Without employing amplitude information, DOPC successfully refocuses light through scattering media with only phase information, making it distinct from the traditional OPC method. This phenomenon sparks our interest in the influence of amplitude information on OPC light refocusing. Therefore, we name OPC light refocusing with and without amplitude information as EAOPC and CAOPC, respectively, and conduct simulations to investigate their differences.

To accurately and efficiently model light scattering and refocusing by OPC, which involves wave-optical phenomena and large-scale simulations, we introduce the PSTD method. The PSTD method numerically solves Maxwell's equations, making it rigorous for modeling wave-optical phenomena. In addition, it leverages the fast Fourier transform for spatial discretization, ensuring high efficiency for large-scale problems based on the Nyquist sampling theorem. Next, we select appropriate simulation parameters to minimize numerical dispersion and maintain numerical stability. Furthermore, simple soft sources are implemented by a compacted source condition to mitigate the Gibbs phenomenon. Finally, we incorporate a PML absorbing boundary condition with the PSTD method to prevent artificial reflections and simulate an infinite space.

We robustly model the OPC phenomenon by dividing it into forward and backward scenarios. Subsequently, we perform simulations of light refocusing using EAOPC and CAOPC in scattering media, where the number of scatterers varies from 100 to 1600. Finally, we analyze the variations between EAOPC and CAOPC, leading to three key findings. First, EAOPC outperforms CAOPC under the same scatterer number density. Second, the performance of EAOPC declines with increasing scatterer number density. Third, CAOPC is applicable in dense media but not in sparse media.

The reasons behind the findings are also discussed. EAOPC delivers better performance than CAOPC because it applies a better amplitude distribution scheme. The reduction of EAOPC performance under higher scatterer number densities is due to the increased complexity of the medium. Finally, owing to the uniformity of scattered waves in dense media, CAOPC presents similar behavior and comparable performance to EAOPC. However, in sparse media, the scattered waves are not uniform, causing CAOPC to perform differently and making it incomparable to EAOPC. Therefore, since EAOPC requires additional amplitude modulation, CAOPC can serve as a feasible alternative for simpler and more computationally efficient implementations in dense media.

5.2 Future Work

To further develop the insights obtained from this study, future research can be categorized into two directions: simulation-based and experiment-based investigations. The simulation direction aims to deepen the theoretical understanding of OPC light refocusing and provide a more comprehensive picture of light manipulation in scattering media. In contrast, the experimental direction aims to evaluate the practical feasibility of EAOPC and CAOPC, thereby advancing their applicability in optical systems.

doi:10.6342/NTU202501087

Building on the current PSTD simulations, future work can explore different simulation scenarios to expand the knowledge of EAOPC and CAOPC further. First, the two factors that affect light scattering most are scatterers and wavelength. Hence, expanding simulations to varying cylinder radius or refractive index and different wavelengths can reveal how structural complexity and spectral dependencies influence the performance of EAOPC and CAOPC. Additionally, future work may investigate EAOPC and CAOPC light refocusing in biological tissues by changing cylinders to cells and incorporating optical absorption. Finally, although the amplitude distribution strategy of EAOPC makes its performance better than that of CAOPC, we are currently unable to confirm whether the strategy represents the optimal amplitude distribution strategy. Future studies may aim to either discover a more effective amplitude distribution strategy or establish theoretical proof to support the optimality of EAOPC's amplitude distribution strategy, which could significantly advance the understanding of OPC.

For experiment-based investigations, implementing the simulation findings is a crucial next step. The CAOPC technique can be realized using an SLM and a CCD camera. In this configuration, the SLM modulates the phase of a constant-amplitude beam based on the feedback information from the CCD camera. This setup avoids the complexity of amplitude modulation, offering a simple and accessible approach to light refocusing. Building upon this setup, it is possible to extend the system to simultaneously modulate both phase and amplitude from the feedback information, thereby realizing the EAOPC technique. EAOPC enables superior light refocusing through scattering media. Applying EAOPC in biological tissues could enhance diagnostic and therapeutic applications, such as optical imaging and phototherapy, improving the performance of biophotonics technologies. As a result, in future experimental developments, the choice between CAOPC and EAOPC may depend on specific application requirements. CAOPC may be

doi:10.6342/NTU202501087

more suitable for scenarios where system simplicity and computational efficiency are prioritized, while EAOPC may be preferable in applications where more effective light refocusing is essential.

Overall, these simulation-based investigations seek to enhance our comprehension of OPC light refocusing, while experiment-based investigations seek to implement the simulation findings. The long-term goal is to fully understand light propagation in complex scattering media and apply this knowledge to manipulate light in biological tissues, where effective light focusing remains a significant challenge. Ultimately, these efforts could open up new possibilities for advanced biophotonics applications.

doi:10.6342/NTU202501087

REFERENCE

[1] A. P. Mosk, A. Lagendijk, G. Lerosey, and M. Fink, "Controlling waves in space and time for imaging and focusing in complex media," *Nature photonics,* vol. 6, no. 5, pp. 283-292, 2012.

[2] R. Horstmeyer, H. Ruan, and C. Yang, "Guidestar-assisted wavefront-shaping methods for focusing light into biological tissue," *Nature photonics,* vol. 9, no. 9, pp. 563-571, 2015.

[3] H. Ruan, J. Xu, and C. Yang, "Optical information transmission through complex scattering media with optical-channel-based intensity streaming," *Nature Communications,* vol. 12, no. 1, p. 2411, 2021.

[4] H. Cao, A. P. Mosk, and S. Rotter, "Shaping the propagation of light in complex media," *Nature Physics,* vol. 18, no. 9, pp. 994-1007, 2022.

[5] C.-Y. Shen, J. Li, T. Gan, Y. Li, M. Jarrahi, and A. Ozcan, "All-optical phase conjugation using diffractive wavefront processing," *Nature Communications,* vol. 15, no. 1, p. 4989, 2024.

[6] I. M. Vellekoop and A. P. Mosk, "Focusing coherent light through opaque strongly scattering media," *Optics letters,* vol. 32, no. 16, pp. 2309-2311, 2007.

[7] M. Cui and C. Yang, "Implementation of a digital optical phase conjugation system and its application to study the robustness of turbidity suppression by phase conjugation," *Optics express,* vol. 18, no. 4, pp. 3444-3455, 2010.

[8] I. M. Vellekoop, M. Cui, and C. Yang, "Digital optical phase conjugation of fluorescence in turbid tissue," *Applied physics letters,* vol. 101, no. 8, 2012.

[9] L. Liu *et al.*, "Anti-scattering light focusing with full-polarization digital optical phase conjugation based on digital micromirror devices," *Optics Express,* vol. 30, no. 18, pp. 31614-31622, 2022.

[10] Y. Baek, H. B. de Aguiar, and S. Gigan, "Phase conjugation with spatially incoherent light in complex media," *Nature Photonics,* vol. 17, no. 12, pp. 1114-1119, 2023.

[11] P. Wang *et al.*, "Toward optimal performance of systems for digital optical phase conjugation," *Physical Review Applied,* vol. 21, no. 1, p. 014004, 2024.

[12] S. H. Tseng and C. Yang, "2-D PSTD Simulation of optical phase conjugation for turbidity suppression," *Optics express,* vol. 15, no. 24, pp. 16005-16016, 2007.

[13] S. H. Tseng, "2-D PSTD Simulation of focusing monochromatic light through a macroscopic scattering medium via optical phase conjugation," *Biomedical Optics Express,* vol. 6, no. 3, pp. 815-826, 2015.

[14] Q. H. Liu, "Large-scale simulations of electromagnetic and acoustic measurements using the pseudospectral time-domain (PSTD) algorithm," *IEEE Transactions on Geoscience and Remote Sensing,* vol. 37, no. 2, pp. 917-926, 1999.

[15] G.-X. Fan, Q. H. Liu, and S. A. Hutchinson, "FDTD and PSTD simulations for plasma applications," *IEEE transactions on plasma science,* vol. 29, no. 2, pp. 341-348, 2001.

[16] P. A. Franken, A. E. Hill, C. W. Peters, and G. Weinreich, "Generation of optical harmonics," *Physical review letters,* vol. 7, no. 4, p. 118, 1961.

[17] D. M. Pepper, "Applications of optical phase conjugation," *Scientific American,*

doi:10.6342/NTU202501087

vol. 254, no. 1, pp. 74-83, 1986.

[18] G. S. He, "Optical phase conjugation: principles, techniques, and applications," *Progress in Quantum Electronics,* vol. 26, no. 3, pp. 131-191, 2002.

[19] X. Xu, H. Liu, and L. V. Wang, "Time-reversed ultrasonically encoded optical focusing into scattering media," *Nature photonics,* vol. 5, no. 3, pp. 154-157, 2011.

[20] Z. Cheng and L. V. Wang, "Focusing light into scattering media with ultrasound-induced field perturbation," *Light: Science & Applications,* vol. 10, no. 1, p. 159, 2021.

[21] C.-L. Hsieh, Y. Pu, R. Grange, G. Laporte, and D. Psaltis, "Imaging through turbid layers by scanning the phase conjugated second harmonic radiation from a nanoparticle," *Optics express,* vol. 18, no. 20, pp. 20723-20731, 2010.

[22] Y. M. Wang, B. Judkewitz, C. A. DiMarzio, and C. Yang, "Deep-tissue focal fluorescence imaging with digitally time-reversed ultrasound-encoded light," *Nature communications,* vol. 3, no. 1, p. 928, 2012.

[23] L. Wang, S. L. Jacques, and L. Zheng, "MCML—Monte Carlo modeling of light transport in multi-layered tissues," *Computer methods and programs in biomedicine,* vol. 47, no. 2, pp. 131-146, 1995.

[24] D. A. Boas, J. P. Culver, J. J. Stott, and A. K. Dunn, "Three dimensional Monte Carlo code for photon migration through complex heterogeneous media including the adult human head," *Optics express,* vol. 10, no. 3, pp. 159-170, 2002.

[25] S. H. Tseng and B. Huang, "Comparing Monte Carlo simulation and pseudospectral time-domain numerical solutions of Maxwell’s equations of light scattering by a macroscopic random medium," *Applied Physics Letters,* vol. 91, no. 5, 2007.

[26] K. Yee, "Numerical solution of initial boundary value problems involving Maxwell's equations in isotropic media," *IEEE Transactions on antennas and propagation,* vol. 14, no. 3, pp. 302-307, 1966.

[27] A. Taflove and S. C. Hagness, *Computational electromagnetics: the finite-difference time-domain method*, 3 ed. Artech House Publishers, 2005.

[28] A. K. Dunn, C. L. Smithpeter, A. J. Welch, and R. R. Richards-Kortum, "Finite-difference time-domain simulation of light scattering from single cells," *Journal of Biomedical Optics,* vol. 2, no. 3, pp. 262-266, 1997.

[29] R. Drezek, A. Dunn, and R. Richards-Kortum, "Light scattering from cells: finite-difference time-domain simulations and goniometric measurements," *Applied optics,* vol. 38, no. 16, pp. 3651-3661, 1999.

[30] R. Drezek, A. Dunn, and R. Richards-Kortum, "A pulsed finite-difference time-domain (FDTD) method for calculating light scattering from biological cells over broad wavelength ranges," *Optics Express,* vol. 6, no. 7, pp. 147-157, 2000.

[31] Q. H. Liu, "The PSTD algorithm: A time-domain method requiring only two cells per wavelength," *Microwave and optical technology letters,* vol. 15, no. 3, pp. 158-165, 1997.

[32] T.-W. Lee and S. C. Hagness, "A compact wave source condition for the pseudospectral time-domain method [EM wave propagation applications]," *IEEE Antennas and wireless propagation letters,* vol. 3, pp. 253-256, 2004.

[33] J.-P. Berenger, "A perfectly matched layer for the absorption of electromagnetic waves," *Journal of computational physics,* vol. 114, no. 2, pp. 185-200, 1994.

[34] Z. S. Sacks, D. M. Kingsland, R. Lee, and J.-F. Lee, "A perfectly matched anisotropic absorber for use as an absorbing boundary condition," *IEEE transactions on Antennas and Propagation,* vol. 43, no. 12, pp. 1460-1463, 1995.